

# Adjoint-based shape optimization of a ship hull using a Conditional Variational Autoencoder (CVAE) assisted propulsion surrogate model

Moloud Arian Maram<sup>a,b,\*</sup>, Georgios Bletsos<sup>b,\*\*</sup>, Thanh Tung Nguyen<sup>a</sup>, Ahmed Hassan<sup>b</sup>, Michael Palm<sup>a</sup>, Thomas Rung<sup>b</sup>

<sup>a</sup>*J.M. Voith SE & Co. KG, Alexanderstrasse*

*2, Heidenheim, 89522, Baden-Württemberg, Germany*

<sup>b</sup>*Institute for Fluid Dynamics and Ship Theory, Hamburg University of Technology, Am Schwarzenberg-Campus 4, Hamburg, 21073, , Germany*

---

## Abstract

Adjoint-based shape optimization of ship hulls is a powerful tool for addressing high-dimensional design problems in naval architecture, particularly in minimizing the ship resistance. However, its application to vessels that employ complex propulsion systems introduces significant challenges. They arise from the need for transient simulations extending over long periods of time with small time steps and from the reverse temporal propagation of the primal and adjoint solutions. These challenges place considerable demands on the required storage and computing power, which significantly hamper the use of adjoint methods in the industry. To address this issue, we propose a machine learning-assisted optimization framework that employs a Conditional Variational Autoencoder-based surrogate model of the propulsion system. The surrogate model replicates the time-averaged flow field induced by a Voith Schneider Propeller and replaces the geometrically and time-resolved propeller with a data-driven approximation. Primal flow verification examples demonstrate that the surrogate model achieves significant computational savings while maintaining the necessary accuracy of the resolved propeller. Optimization studies show that ignoring the propulsion system can yield de-

---

The first two authors contributed equally to this work and share corresponding author responsibilities.

\*Corresponding author: moloud.arianmaram@voith.com

\*\*Corresponding author: george.bletsos@tuhh.de

signs that perform worse than the initial shape. In contrast, the proposed method produces shapes that achieve more than an 8% reduction in resistance.

*Keywords:* Adjoint-based Shape Optimization, Machine Learning based Surrogate Models, Conditional Variational Autoencoder (CVAE), Voith Schneider propulsion (VSP), Self-propelled Ship, Propulsion Model, Hull Optimization

---

## 1. Introduction

Shipping is one of the most popular modes of transportation, accounting for more than 80% of global trade by volume [1]. However, it also contributes significantly to greenhouse gases,  $\text{NO}_x$  and  $\text{SO}_x$  emissions, which pose severe environmental concerns [2, 3]. Reducing the environmental footprint of shipping by increasing the hydrodynamic or propulsion efficiency can substantially reduce the fuel-related pollutant emissions of marine vessels [4], and therefore has become a priority for shipbuilding. This has led to a growing interest in optimizations of the hull shape and the integration of the propeller in order to minimize the resistance and/or improve the propulsion efficiency, e.g. [5, 6, 7, 8, 9]. To this end, adjoint-based methods have become essential due to their ability to compute gradients at a cost nearly independent of the number of design variables [10]. In marine applications, Springer and Urban proposed an adjoint-based framework for rigid body motion in multi-phase flows, requiring only two static flow simulations [11]. Nazemian et al. achieved resistance reductions through adjoint solvers and mesh morphing [12, 13], while Brenner et al. [14] integrated parametric modeling with CFD adjoint solvers to enable rapid sensitivity analysis. Kühl et al. advanced the field by a consistent two-phase-flow method for free floating vessels, introducing a node-based adjoint method using the Steklov–Poincaré metric and improving solver stability on unstructured grids through elliptic relaxation [9, 15, 16]. All these examples refer to steady-state optimizations and usually neglect propulsion influences.

The present study focuses on a marine vessel equipped with a Voith Schneider Propeller (VSP), cf. Fig. 1. The propulsion system can generate omnidirectional thrust through a cyclic blade motion [17, 18]. Unlike conventional screw propellers, the VSP operates with blades rotating and simultaneously pitching in a vertical plane. The complex kinematics induces unsteady,

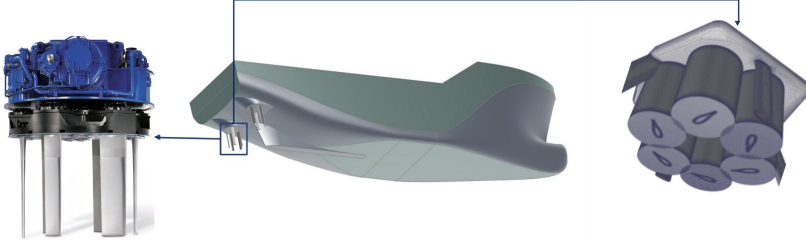


Figure 1: Service Operation Vessel equipped with a Voith Schneider Propeller and exemplary mesh components.

spatially complex flow features, strong vortex shedding with pronounced blade–vortex interactions and pressure fluctuations [19, 20, 21, 22, 23, 24].

This presents two methodological challenges that adversely affect their numerical resolution in large-scale optimization applications:

1. A direct resolution of the rotating propeller would require unsteady adjoint simulations. These are difficult to perform due to the adjoint backward integration in time and the corresponding need to store the complete history of the primal flow field.

In case of large simulations with tens of millions of spatial grid points and hundreds of thousands of time steps, this is either unfeasible or yields an unacceptable reduction in computational efficiency for massively parallel applications on current high-performance computers. Proposed solutions are mostly based on check-pointing strategies, e.g. [25, 26, 27, 28]. These recompute a temporal segment of the primal solution starting from a nearby check-point and represent a compromise between computational and memory effort. However, the associated algorithmic effort and the considerable computational demands often limit their practical applicability. An innovative alternative refers to singular value decomposition (SVD) methods, for constructing reduced-order models, e.g. [29]. In the context of industrial adjoint shape optimizations, such lossy compression approaches must be implemented in a time-incrementing [30, 31, 32, 33, 34, 35, 36] and parallel manner [37].

2. Another critical aspect results from the broad spectrum of relevant time scales and the resulting large ratio of the total simulation duration to

the time-step size. In naval engineering, this becomes particularly clear with the example of a free-floating ship: There, the time scale of the ship motion is several orders of magnitude larger than the time scale of the flow around the propeller. To reduce the associated effort, industrial CFD simulations often use multiple reference frames (MRFs) to simulate the flow around rotating components [38]. Adjoint-based studies using MRF methods to optimize wind turbines and ducted hydrokinetic devices are published in [39, 40]. Due to the perpendicular alignment of the cruise direction and the axis of rotation as well as the complex kinematics, the MRF concept is not applicable to the VSP. An even simpler approach is the use of actuator-disc or body-force models to represent the propulsion. Such adjoint hull shape optimization approaches have been published in [41, 7]. While actuator-disc surrogate models have proven effective for axial flows through screw-type rotors, they are not directly applicable to cycloidal systems such as the VSP.

Within the framework of an adjoint analysis, the simulation of the resolved or modeled VSP is therefore challenging. However, the influences of propulsion on the desired optimal shapes are of great importance. This can be seen, for example in Section 6, where an optimization neglecting the propeller yields a hull shape that in fact results in an increased resistance when assessed under propulsion conditions. This typically also changes the load distribution across the hull surface, which –in turn– can significantly influence both the floating position and the required propulsion power.

### 1.1. Suggested Optimization Approach

Due to the aforementioned challenges in resolving the VSP propeller, we suggest an AI-assisted framework that integrates a machine learning (ML)-based surrogate model of the propulsor into a continuous adjoint-based shape optimization process. Rather than geometrically resolving the unsteady interaction between the propeller and the hull, a generative neural network is trained on time-averaged unsteady CFD data to emulate the propeller-induced (time-averaged) flow field.

ML-based fluid dynamic applications have undergone an impressive development in the past. Recent studies demonstrate that ML-based models can reproduce turbulent flow fields with high accuracy while significantly reducing computational costs, see e.g. Vinuesa et al. [42], Duraisamy et al. [43] or Brunton et al. [44, 45]. Similarly, Thuerey et al. [46] demonstrated

that generative networks can accurately predict complex 3D flow fields with minimal computational effort. In contrast to purely data-driven methods, physics-informed neural networks (PINNs) are frequently used to include physical constraints in the learning process [47, 48, 49].

The learning strategy employed in this work follows previously published data-driven methods for learning complex fluid dynamic fields using Convolutional Neural Networks (CNNs) [50, 51, 52, 53]. However, in this work, machine-learning information is not used for a rapid, parameter-based evaluation of designs – for example, in the context of onboard decision support systems [52, 54] – but serves to support a flow simulation and adjoint analysis by adopting a Conditional Variational Autoencoder (CVAE) to learn the VSP-induced velocity field. In contrast to other autoencoder models, the CVAE features a latency space enriched with so-called labels, which are used to parameterize the fields to be learned. The enrichment replaces the additional fully connected neural networks that are used to map the parameters (labels) to the latent space suggested in other studies [50, 52, 53, 55]. In this work, we employ 11 labels, i.e. ten geometric parameters and one operating parameter that captures the cruising speed. Similar frameworks have been successfully applied in wind turbine condition monitoring, where CNN-based CVAEs effectively captured parameter–response relationships [56]. In the present investigation, the approach in [56] is extended by incorporating residual blocks and self-attention mechanisms to enhance the accuracy of the output.

The transfer between the learned data and the optimization study is restricted to the flow velocities through the use of a meta grid. The latter extends over a circular cylindrical domain that extends slightly beyond the area swept by the propeller. By configuring the 11 data labels, the velocities are derived from the ML-based surrogate model at the discrete meta-mesh points. The information is subsequently interpolated to the CFD mesh used for the optimization studies, which does not resolve the propeller. The introduction of ML-based velocities into the momentum equations uses an implicit enforcement. This not only enables a robust, tightly coupled treatment, which, in particular, eliminates the need to guarantee strictly continuity-compatible ML velocity fields, but also offers high flexibility in meshing. All other flow variables, i.e., pressure and turbulence variables, follow from their respective governing equations without any changes. Building on this foundation, the model is tailored to efficiently handle a range of geometries and operating

conditions, while preserving design sensitivity with sufficient accuracy.

The remainder of this paper is organized as follows: Section 2 details the methodology, including the development of the surrogate model, presenting the dataset generation, surrogate validation and integration to the CFD solver. The section closes with the detailed description of the employed adjoint-based optimization strategy. Section 3 describes the application of the proposed framework to a self-propelled hull optimization problem and performance assessment. Section 4 concludes with a summary of findings and discusses broader implications for CFD-based design in marine engineering.

## 2. Autoencoder Surrogate Model

The current study uses an autoencoder (AE), which is composed of an encoder and a decoder, as illustrated in Fig. 2. The encoder maps the input  $\mathbf{x} \in \mathbb{R}^N$  to a usually lower dimensional latent space representation  $\mathbf{z} \in \mathbb{R}^m$  and the decoder subsequently maps  $\mathbf{z}$  to the full dimension to obtain a reconstruction of the input,  $\hat{\mathbf{x}} \in \mathbb{R}^N$ . Here  $N$  is the total number of meta mesh grid points, and we consider 3 input vectors, which are the three Cartesian velocities. The encoder and decoder usually feature symmetric structures. All models in this work are based on a convolutional autoencoder (CAE), as the convolutional layers are usually better than fully connected layers at capturing spatial dependencies.

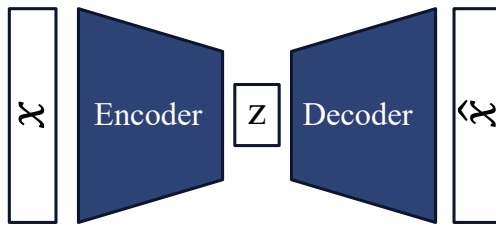


Figure 2: Basic autoencoder scheme.

In particular, a Conditional Variational Autoencoder is employed as a surrogate model to approximate the velocity field in the vicinity of the VSP. Similar to the standard Variational Autoencoder (VAE), the CVAE is probabilistic and maps each input to a distribution parameterized by a mean and a variance, where the encoder performs stochastic sampling in the latent space and the decoder reconstructs or generates new flow fields from these

samples [57]. As illustrated in Fig. 3, the encoder therefore provides two outputs, a mean  $\boldsymbol{\mu} \in \mathbb{R}^m$  and a diagonal covariance matrix  $\boldsymbol{\Sigma} \in \mathbb{R}^{m \times m}$ , where the diagonal entries are  $(\sigma_i)^2, i \in \{1, \dots, m\}$  and the log-variance  $\log(\boldsymbol{\sigma}^2)$  is utilized for stability reasons. The latent space representations are forced to follow a probability distribution, which is assumed to be normally distributed:  $\mathbf{z} \sim \mathcal{N}(\boldsymbol{\mu}, \boldsymbol{\Sigma})$ , using  $\boldsymbol{\sigma} = \exp(0.5 \cdot \log(\boldsymbol{\sigma}^2))$  and generating  $\boldsymbol{\epsilon} \sim \mathcal{N}(\mathbf{0}, \mathbf{I})$ , the computation of latent variables reads  $\mathbf{z} = \boldsymbol{\mu} + \boldsymbol{\sigma} \odot \boldsymbol{\epsilon}$ .

Unlike the conventional VAE, however, the CVAE conditions both the encoder and the decoder on auxiliary inputs, enabling controlled generation of flow fields based on physical parameters. This conditioning mechanism is illustrated in the lower row of the encoder section in Fig. 3, and allows the surrogate model to learn a mapping from label–data pairs to flow-field distributions, thereby producing physically consistent outputs under new operating conditions.

The training objective of the CVAE is defined through a composite loss function that balances two competing goals: reconstruction accuracy and latent-space regularization. The reconstruction loss is computed using the Mean Squared Error (MSE). It measures the difference between the predicted  $\hat{\mathbf{x}}$  and reference flow fields  $\mathbf{x}$ , enforcing accurate reproduction of flow features, viz.

$$\text{MSE} = \frac{1}{N} \sum_{i=1}^N (x_i - \hat{x}_i)^2. \quad (1)$$

To ensure a smooth and continuous latent representation, the Kullback–Leibler (KL) divergence term penalizes deviations of the learned latent distribution  $q(\mathbf{z}|\mathbf{x})$  from the prior distribution  $p(\mathbf{z}) = \mathcal{N}(\mathbf{0}, \mathbf{I})$ , i.e.

$$D_{KL}(q(\mathbf{z}) \parallel p(\mathbf{z})) = \frac{\beta}{2} \left[ \text{tr}(\boldsymbol{\Sigma}) + \boldsymbol{\mu}^\top \cdot \boldsymbol{\mu} - k - \log |\boldsymbol{\Sigma}| \right], \quad \beta > 0 \quad (2)$$

where  $k$  is the dimensionality of the latent space. In the current study  $k = 2$  and  $\beta = 1$ . For  $\beta = 1$ , this is referred to as the VAE [58] and  $\beta \neq 1$  denotes the  $\beta$ -VAE [59]. The total loss function is formulated as

$$L = \text{MSE} + D_{KL}(q(\mathbf{z}) \parallel p(\mathbf{z})), \quad (3)$$

This composite loss ensures both an accurate flow-field reconstruction and a structured, continuous latent space suitable for interpolation and generalization.

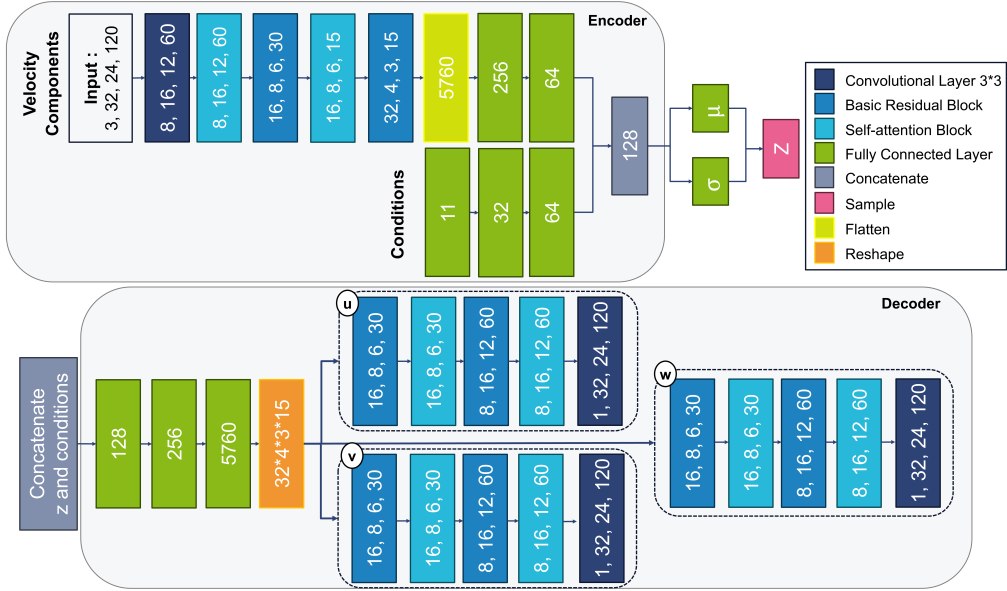


Figure 3: Architecture of the CVAE model used to reconstruct the velocity field.

## 2.1. Configuration of the Conditional Variational Autoencoder

Figure 3 illustrates the architecture of the proposed Conditional Variational Autoencoder. The encoder processes a multi-channel 3D velocity input along with the conditioning vector, utilizing a combination of convolutional layers, residual blocks, self-attention mechanisms, and fully connected layers. The conditioning vector is processed separately through fully connected layers and then appended to the encoded features. This combined representation is mapped to the latent space, producing the mean and standard deviation required for the reparameterization trick [58], which enables differentiable stochastic training.

The decoder mirrors the encoder architecture with slight modifications. The latent vector, fused with the conditioning variables, is expanded through fully connected layers and reshaped. Since the three velocity components differ by several orders of magnitude, the conditioning variables are processed separately through three parallel branches, each composed of convolutional layers, self-attention modules, and residual blocks, dedicated to reconstructing one velocity component. Finally, the reconstructed velocity components are concatenated.

Self-attention mechanisms, such as the non-local operation introduced by

Wang et al. [60], adaptively emphasize important spatial regions by weighting features based on global contextual relevance. Originally developed for natural language processing [61], self-attention has been effectively applied in computational fluid dynamics to model non-local flow phenomena such as vortex shedding and flow separation. Peng et al. [62] demonstrated its ability to capture long-range flow dependencies, Wu et al. [63] employed it within a convolutional autoencoder for improved flow reconstruction, and Schwarz et al. [55] applied attention-based networks to predict fluid dynamic loads. Figure 4a illustrates the self-attention mechanism. The query (Q) and key (K) matrices determine the relevance between different spatial locations through their dot-product similarity, while the value (V) matrix contains the corresponding feature information to be aggregated. This mechanism allows the network to selectively focus on important regions by weighting the value features according to the query-key attention scores.

Residual blocks facilitate the training of deeper networks by enabling stable gradient propagation [64]. Schematic representations of the self-attention mechanism and residual block are provided in Figure 4b. A typical block consists of two or more consecutive convolutional layers (Conv), each followed by batch normalization (BN) and a nonlinear activation function, such as ReLU in the present study.

## 2.2. Learning Rate

The learning rate is a key hyperparameter that controls the step size for updating model weights during training. To ensure both stability and efficient convergence, a 1-cycle learning rate schedule [65] is generally employed over 1200 training epochs. The learning rate is initially set to  $1 \cdot 10^{-4}$ , peaks at  $2 \cdot 10^{-4}$  by epoch 200, and gradually decreases to  $5 \cdot 10^{-6}$  by the end of training. The model is optimized using the Adam algorithm [66] with a mini-batch size of 4. Our preliminary investigations indicated that a latent dimension of two provided the best trade-off between reconstruction accuracy and model generalization.

## 3. CFD-based Methodology

To construct the surrogate model, a CFD-based dataset was generated through transient numerical simulations. To limit the effort, the current research is confined to single-phase flows around ships in a fixed floating position. The training, validation, and test data refer to a sequence of offline

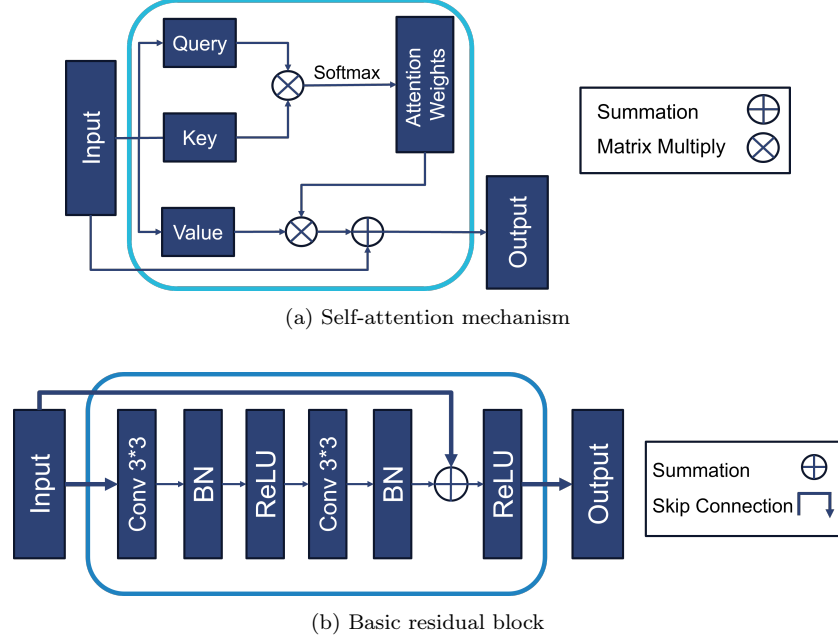


Figure 4: Architecture of self-attention mechanism (top) and basic residual block (bottom).

simulations of the full-scale flow around a 92-meter-long Service Operation Vessel (SOV). The vessel is equipped with two five-bladed Voith Schneider propellers. Each VSP has a diameter of 2.65 meters and a blade length of 2.30 meters, and operates at a rotational speed of 79.28 rpm. The SOV cruises forward at 6.7–8.1 m/s, which yields a Reynolds number of  $Re = 4.1 - 4.9 \cdot 10^8$  based on the length of the vessel and the cruising speed. Since we only consider single-phase flows, the elevation of the free surface is neglected, i.e., a Froude number of  $Fn = 0$ .

### 3.1. Governing Equations

The offline simulations solve the three-dimensional, single-phase Reynolds-Averaged Navier–Stokes (RANS) equations, viz.

$$R^p = \frac{\partial v_i}{\partial x_i} = 0 \quad (4)$$

$$R_i^v = \rho \left[ \frac{\partial v_i}{\partial t} + v_k \frac{\partial v_i}{\partial x_k} \right] + \frac{\partial}{\partial x_k} [p^{\text{eff}} \delta_{ik} - 2\mu^{\text{eff}} S_{ik}] = 0, \quad (5)$$

where,  $v_i$  and  $p^{\text{eff}}$  correspond to the Reynolds-averaged velocity components and pressure, with the latter being augmented by the turbulent kinetic energy ( $k$ ) term,  $2\rho k/3$ . The symbol  $\delta_{ik}$  denotes the Kronecker delta. Based on the Boussinesq hypothesis, the effective viscosity  $\mu^{\text{eff}} = \mu + \mu^t$  of turbulent flows consists of the molecular viscosity and the turbulent contribution, which is identified by the solution of a two-equation turbulence model. The components of the strain-rate tensor  $S_{ik}$  are defined as

$$S_{ik} = \frac{1}{2} \left( \frac{\partial v_i}{\partial x_k} + \frac{\partial v_k}{\partial x_i} \right), \quad (6)$$

Numerical results are obtained from a standard pressure-based, cell-centered finite volume method [67]. The approach is second-order accurate in space and time and capable of processing unstructured polyhedral meshes. The segregated procedure iterates the fields to convergence using a pressure-correction scheme.

### 3.2. Computational Domain and Numerical Mesh

The computational domain of the offline simulations includes a half-hull representation of the submerged portion of the vessel, which is equipped with a Voith–Schneider propeller comprising five blades, each with a blade length  $L_{\text{VSP}} = 2.3$  m and a radius  $r_{\text{VSP}} = 1.33$  m. Boundary conditions are defined to reduce artificial reflections and maintain physical fidelity. A velocity inlet is located two ship lengths (LOA) upstream of the aft perpendicular, and a pressure outlet is placed two LOA downstream. A symmetry boundary condition is applied at the ship centerline. The lateral far-field boundary, located at 1.5 LOA from the centerline in the  $y$ -direction, is modeled as a slip wall. The hull surface is treated as a no-slip wall, and the top and bottom boundaries are defined as slip walls, with the bottom surface positioned 1.5 LOA below the waterline. The inflow is aligned with the negative  $x$ -axis. Figure 5 illustrates the computational domain and the VSP-equipped vessel.

A sliding mesh technique is employed to resolve the VSP’s rotation in  $1^\circ$  increments per time step. To ensure accuracy and efficiency, the meshing strategy combines a structured hexahedral mesh around the VSP for capturing fine-scale flow features with an unstructured polyhedral mesh for the rest of the domain. The entire mesh consists of approximately 2.18 million cells and the propeller mesh consists of around 1.3 million cells, respectively. Wall functions are used to resolve the near wall flow, which corresponds to an approximate resolution of  $y^+ \approx O(100)$  along the walls. Figure 6 illustrates

the utilized mesh on the whole domain, the close-up images of the hull, bow, and propeller area.

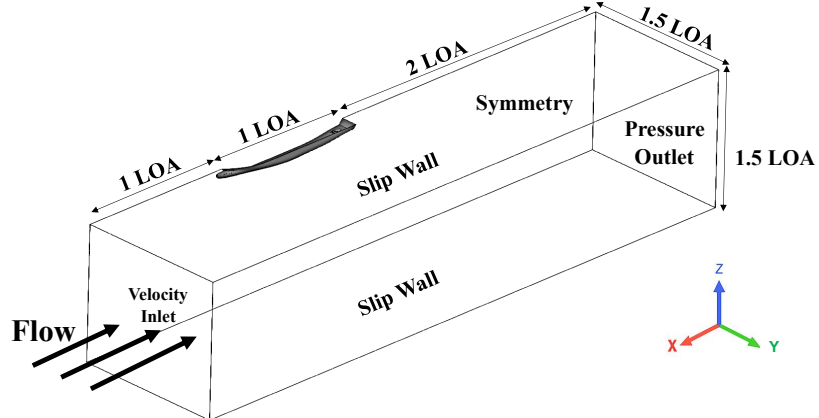


Figure 5: Computational domain and boundary conditions

To resolve the unsteady periodic flow, the simulation captures a periodic segment of  $360^\circ/5$  blades =  $72^\circ$ , corresponding to one-fifth of a full revolution. This segment is discretized using a time-step resolution of  $2^\circ$ . After passing through the initial transient phase, the time-averaged flow field required for training is obtained by averaging the solution over these 36 steps, which effectively represents one complete revolution of the VSP.

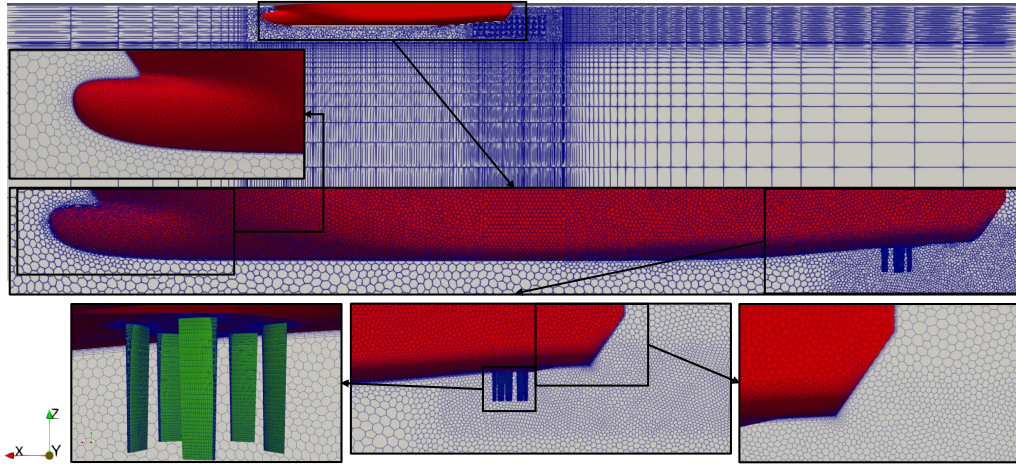


Figure 6: Mesh details of the computational domain around the hull and propeller.

### 3.3. Structure of Parameter Data

To condition the surrogate model, multiple hull geometries, defined by variations of ten geometric parameters, are simulated under three forward speeds, i.e. 6.73, 7.42, 8.11 m/s. The geometric parameters are selected to capture both global and local features of the stern, cf. Fig. 7. The range of values for these parameters is summarized in Table 1. They include the stern deadrise, stern inclination, stern angles Y1 and Y2 (SAY1, SAY2), and five variables related to the so called headbox, a structural extension above the propeller region that serves as a mounting point for the VSP. The latter consist of the front and back lengths (HBLF, HBLB), height (HBH), slope angle (HBAS), and transverse tilt angle (PhiX). HB\_Length is a non-dimensional parameter used to define the length of the headbox relative to the VSP diameter ( $D_{VSP}$ ). The actual headbox length is computed as  $HB\_Length \times D_{VSP}$ . The stern deadrise represents the transverse angle of the hull bottom at the stern, while the stern inclination defines the longitudinal slope of the aft hull section, both of which influence the wake and pressure field near the propeller. This parameterization enables a systematic variation of the aftship and flow-control features throughout the dataset. Note that three geometry parameters, namely the stern deadrise angle, the headbox angle (x), and the headbox length (front), remain frozen in the current study.

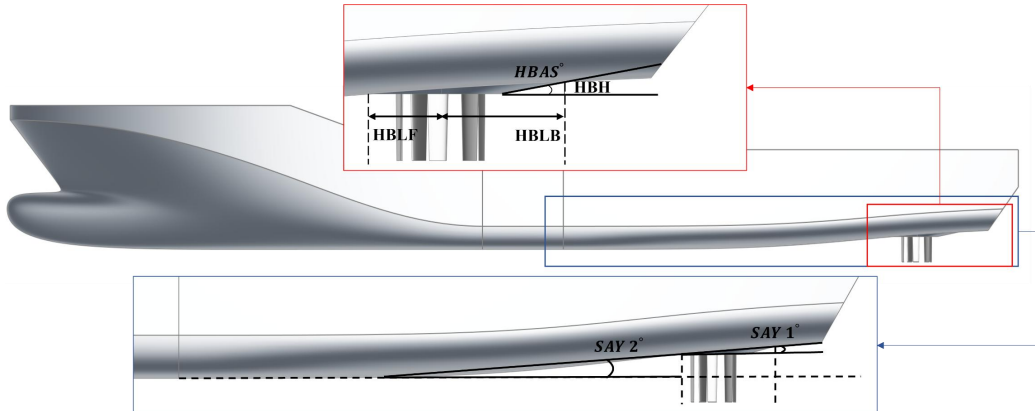


Figure 7: Illustration of the employed geometric parameters, including key aftship and headbox features.

For each simulation, the quality of the solution is ensured based on the convergence of the predicted hull force and propeller thrust.

Table 1: Range of parameters values considered by the data set.

Parameter	Unit	Value Range	Count of Unique Values
Ship Speed (in $x$ -direction)	$m/s$	6.73–8.1	3.0
Stern Deadrise	deg	0.0	1.0
Stern Inclination	deg	0.40–1.40	10.0
Stern Angle Y1 (SAY1)	deg	1.88–6.55	10.0
Stern Angle Y2 (SAY2)	deg	5.29–17.95	10.0
Headbox Length (HB_Length)	-	1.0–2.0	6.0
Headbox Angle X (PhiX)	deg	0.0	1.0
Headbox Angle Slope (HBAS)	deg	6.91–35.38	26.0
Headbox Height (HBH)	m	0.42–1.88	29.0
Headbox Length Back (HBLB)	m	3.81–6.43	18.0
Headbox Length Front (HBLF)	m	2.12	1.0

### 3.4. Meta-Grid

To prepare the communication between the CFD procedures and the surrogate model for the employed machine-learning strategy, a consistent and structured data representation is required. The latter involves a meta-grid which is used to connect the offline CFD-procedures during the training of propulsion influences and the online CFD-procedures during the optimization. To this end, a cylindrical control domain is defined around the VSP. The coordinate system is oriented along the rotational axis of the propeller, with the origin located at the propeller mounting point and the positive axial direction pointing from the blade root toward the blade tip. The domain dimensions are given by  $z = 1.39L_{VSP}$  in the axial direction and  $r = 1.39r_{VSP}$  in the radial direction, capturing flow field variations beyond the blade tip and blade orbit, particularly at the upper axial limit ( $z = 3.1$  m). Figure 8 depicts the extension of the meta grid and its positioning relative to the VSP. Mind that the spacings in the meta grid are deliberately chosen non-equidistant to provide higher resolution in regions where the velocity gradients are larger, particularly in the  $\theta$ -direction.

#### 3.4.1. Integration of offline CFD results into surrogate model

The extraction nodes in the CFD simulation are fixed and defined based on the meta mesh which is overlaid on the computational domain. For each

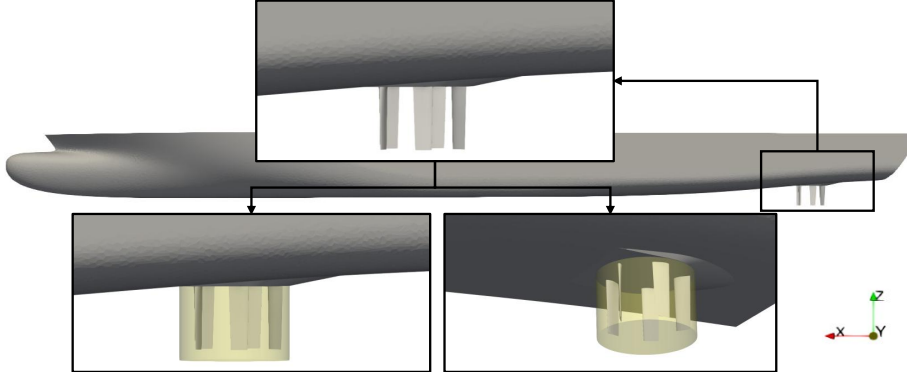


Figure 8: Configuration of the meta-grid around the VSP.

time step, the unstructured CFD data are mapped to the structured meta-grid during training using inverse distance-weighted interpolation [52, 68]. Figure 9 illustrates a sketch of the spacing of the structured meta-grid in a two-dimensional plane. This preserves key flow features while maintaining consistent formatting across all samples. Depending on the blade rotation of the VSP, some nodes at certain time steps lie inside the blade region and therefore are not part of the computational domain. These nodes are excluded for that specific time step during the time-averaging process, where the averaging interval corresponds to one blade period of  $72^\circ$ , with an angular increment of  $2^\circ$ , resulting in a total of 36 time steps. During the time averaging, only the valid nodes (where no blade was present) are taken into account.

#### 3.4.2. Integration of surrogate model into CFD software

The surrogate model should facilitate the simulation-based optimization of hull shapes by seamlessly integrating non-resolved propulsion influences. It outputs the 3D velocity field, given the parameters described in Table 1, in a structured cylindrical meta-grid. To allow for generalization, we consider now a new CFD mesh, outside of the pool of meshes employed for the generation of training, validation, and test data, which discretizes the computational domain without resolving the propeller. Based on the position of the headbox in the computational domain and its inclination w.r.t. the main flow direction, the meta-grid is translated and rotated to the position where the propeller would have been mounted on. Once this transformation is executed, the velocities are mapped from the meta-grid to the new CFD mesh

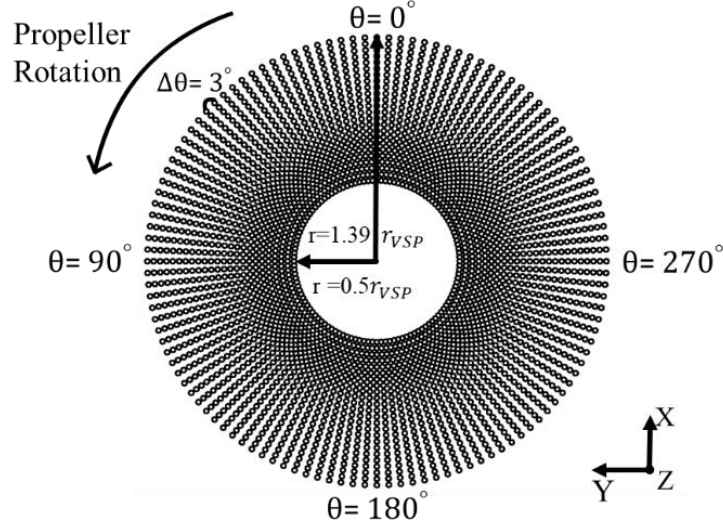


Figure 9: 2D sketch of the meta-grid spacing and angular discretization.

using a nearest-neighbor interpolation, i.e.,

$$\tilde{\phi}(\mathbf{x}) = \phi(\tilde{\mathbf{x}}_j), \quad \text{where } j = \arg \min_i |\mathbf{x} - \tilde{\mathbf{x}}_i| \quad (7)$$

with  $\tilde{\phi}(\mathbf{x})$  denoting the interpolated quantity, here, one of the 3 Cartesian velocity components, at a cell-center  $\mathbf{x}$  of the CFD mesh and  $\phi(\tilde{\mathbf{x}})$  the surrogate model predicted quantity on a cell-center  $\tilde{\mathbf{x}}$  of the meta-grid. The interpolation strategy is only realized for cells in the CFD mesh that lie within the limits of the rotated and translated meta-grid.

Superficially, the integration of the surrogate model into the CFD domain aims to manipulate the solution  $\phi$  at the prescribed location, so that it matches the interpolated output  $\tilde{\phi}$ . A direct approach would simply overwrite the solution at the interpolated cells with  $\tilde{\phi}$ . However, this approach is conceptually flawed because of the strong coupling between the velocity and the other field variables, in particular the pressure. Instead, we apply the approach of solution forcing [67]. In this approach the solution of the RANS equations ( $\phi$ ) is naturally blended with the interpolated quantity ( $\tilde{\phi}$ ) by adding a source term to the discretized momentum equations of the following form

$$A_P \phi_P + \sum_{N(P)} A_N \phi_N = Q_P + \alpha \left[ \rho V (\tilde{\phi} - \phi) \right]_P, \quad (8)$$

where  $\alpha$  stands for a forcing coefficient and  $V$  for the volume of a computational cell with centroid  $P$ . It is easy to see, that  $\alpha$  is not dimensionless, thus making its selection not only problem- but also location- and time- dependent. To avoid this, we modify the forcing in an implicit manner by setting

$$\begin{aligned} A_P \phi_P + \sum_{N(P)} A_N \phi_N &= Q_P + \hat{\alpha} A_P \left[ (\tilde{\phi} - \phi) \right]_P \\ A_P (1 + \hat{\alpha}) \phi_P + \sum_{N(P)} A_N \phi_N &= Q_P + \hat{\alpha} A_P \tilde{\phi}_P, \end{aligned} \quad (9)$$

where  $\hat{\alpha} \geq 0$  is a dimensionless forcing coefficient. Note  $\hat{\alpha} = 0$  is imposed in the cells outside of the limits of the meta-grid. Due to the proportionality of the forcing to the main diagonal coefficient, the implicit forcing approach (9) is space (and time) dependent, in contrast to the explicit approach (8). Moreover, the implicit approach strengthens the main diagonal and thus enhances the robustness of the iterative procedure. Strictly speaking, the condition  $\phi = \tilde{\phi}$  can only be satisfied for (infinitely) large values of  $\alpha$  or  $\tilde{\alpha}$ . However, this is generally undesirable and would indeed be useless, since neither the surrogate model nor the interpolations used are capable of generating divergence-free velocities that are compatible to the discretized continuity equation (4) in the target mesh. The use of PINN strategies to obtain divergence-free meta-grid velocity fields is conceivable, but not very helpful, since even marginal deviations from the divergence-free state can prevent the convergence of the numerical method. Note that the dimensionless property  $\tilde{\alpha}$  is deliberately assigned to values of the order  $O(10^{-1})$  which provides room for deviations from the target field  $\tilde{\phi}$  that are required to preserve the continuity condition (4).

#### 4. Verification and Validation

To assess the capabilities of the surrogate model, a structured training and evaluation procedure was employed. For this purpose, the data set consisting of 180 samples was divided into training (80%), validation (10%), and test subsets (10%). The model was trained using the training set, incorporating both flow field data and the corresponding conditioning labels. A companion validation was conducted every 10 epochs to monitor convergence and mitigate overfitting. After the training, the performance of the model was evaluated using the previously unseen input conditions of the test subset.

#### 4.1. Validation of the Surrogate Model

The results are presented for one representative sample of the test subset. The corresponding parameters for this test sample are summarized in Table 2. The analysis focuses on the axial velocity component, the velocity magnitude

Table 2: Conditioning parameters used for the selected test sample.

Parameter	Unit	Value
Ship Speed ( $x$ -direction)	m/s	7.42
Stern Deadrise	deg	0.0
Stern Inclination	deg	1.067
SAY1	deg	4.99
SAY2	deg	13.87
HB_Length	-	1.2
PhiX	deg	0.0
HBAS	deg	24.88
HBH	m	1.2
HBLB	m	4.42
HBLF	m	2.12

(both normalized by the ship speed), and the divergence of velocity in four axial slices, i.e.,  $z = 0.1, 0.9, 1.7$  and  $z = 2.5$  m below the mounting point of the VSP, within the cylindrical meta-grid domain.

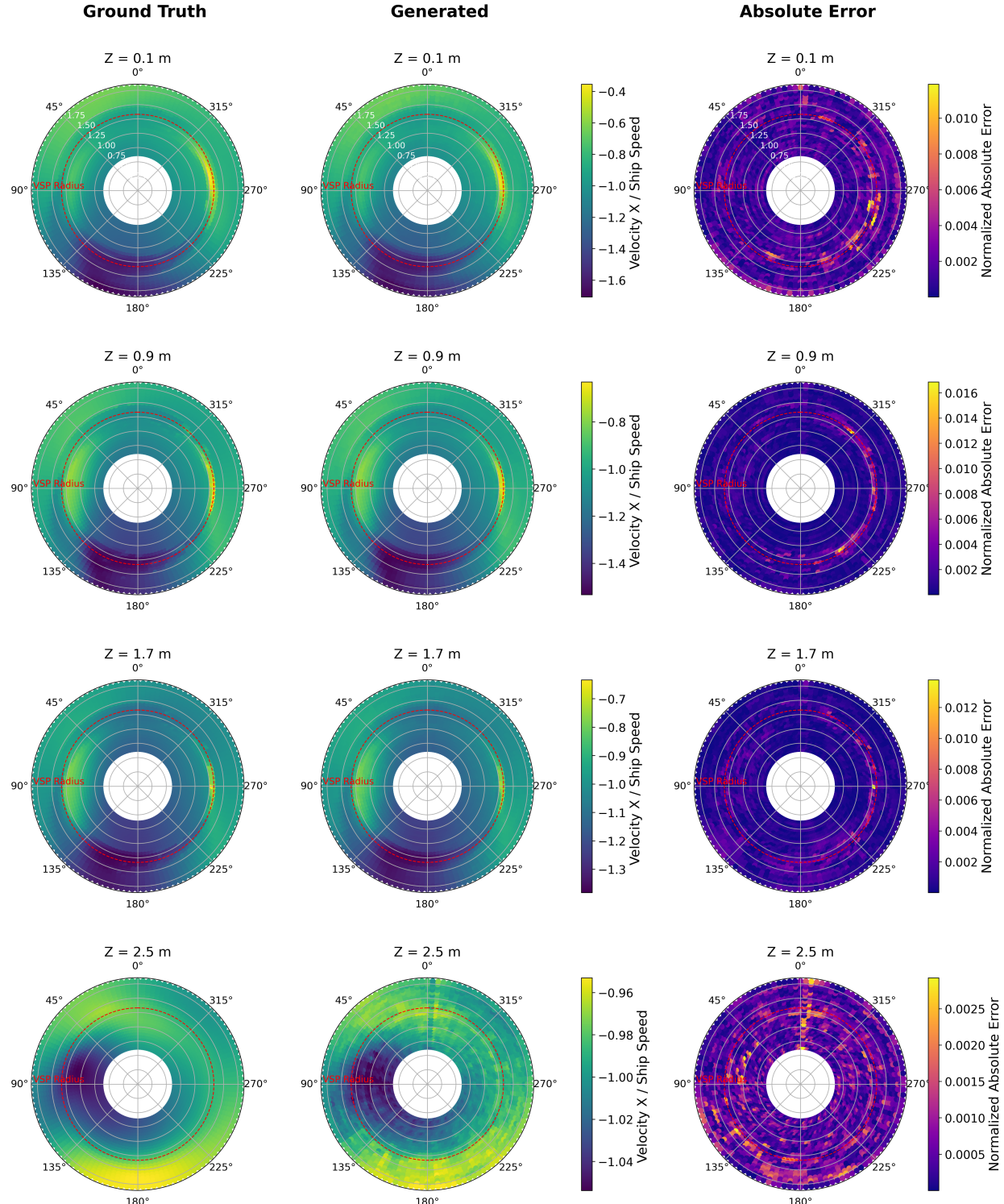
Figures 10 and 11 compare the results of the offline CFD simulations interpolated to the meta-grid (left) with results obtained from the surrogate model (center) and also outline the respective normalized error magnitudes (right). The velocity error is normalized by the ship speed to obtain a relative error metric; this normalization does not imply an increase of the absolute error with increasing ship speed. The contour plots are presented in the local cylindrical coordinate system aligned with the propeller rotational axis. In this representation, the upstream direction corresponds to the top ( $0^\circ$ ) and the downstream direction to the bottom ( $180^\circ$ ). The flow enters the cylindrical domain around the observed, counter-clockwise rotating, port propeller from above ( $0^\circ$ ) and the accelerated flow leaves the domain at the bottom with a slight inclination away from the symmetry plane, i.e., approximately at the  $160^\circ$  location. The dashed red circular line corresponds to the line around which the pitching blades rotate. Mind that the bottom graphs refer to a plane underneath the propeller that is not swept by the propeller

blades, which only reach to  $z = 2.3$  m. The axial velocity  $V_x$  dominates the forward-directed propulsion and also exhibits the largest variations in the domain covered by the meta-grid. Accurately capturing this component is critical for characterizing the thrust and the wake behavior.

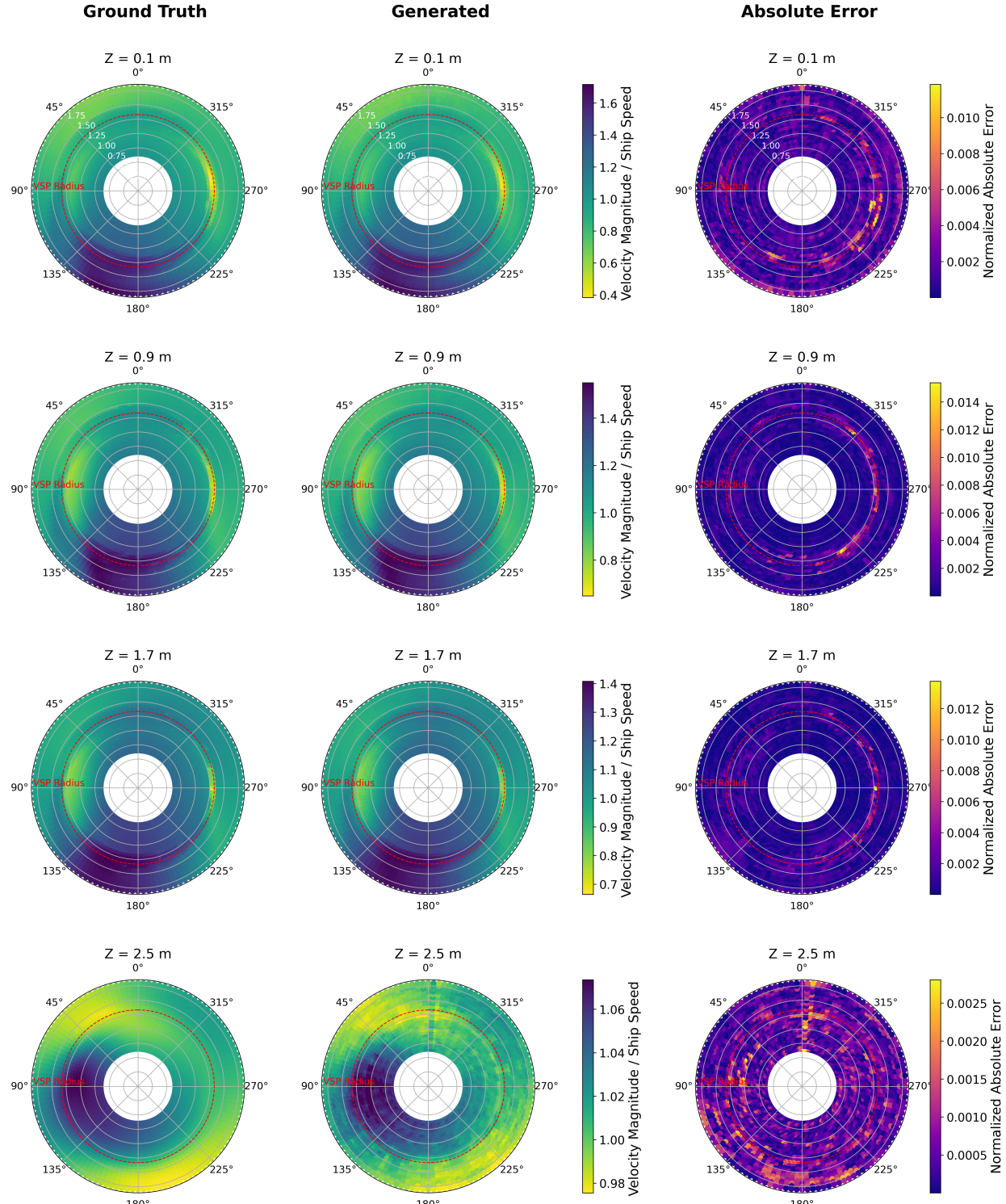
The results displayed demonstrate that the surrogate model reconstructs both global and local flow patterns with high fidelity. The model mimics the generation of axial momentum by the propeller quite well and also captures the areas of strong deceleration near the blade paths. The errors remain locally confined and are typically at a low level of approximately 1–2% of the ship speed. Local maximum errors occur in areas with large spatial gradients and are approximately 10% of the ship’s speed. The error magnitude generally increases closer to the headbox.

Another approach to assess the predicted velocity components is to study the velocity divergence, i.e., how well the velocity field predicted by the surrogate model satisfies the conservation of volume in comparison to the time-averaged interpolated CFD results. Strictly speaking, the unsteady CFD results are conservative, but the time-averaged interpolated CFD results are not necessarily conservative, in particular, if one considers the fluid homogenization of the regions temporarily swept by the propeller blades.

For this purpose, the velocity divergence in the meta-grid was calculated twice, once for the time-averaged CFD data to be learned and once for the predictions of the surrogate model. The resulting contour plots of the velocity divergence and the corresponding error magnitudes for selected  $z$ -planes are presented in Fig. 12, whose structure is similar to that of Figs. 10 and 11. In general, significant non-zero divergence levels are observed. The largest levels are located near the circumference of the rotor (cf. dashed line), while the outer and inner radial zones remain mostly divergence-free. The top plane located near the headbox reveals the largest divergence levels and the bottom plane the smallest levels. Similar to figures 10 and 11, the discrepancy between the interpolated, time-averaged CFD results and the surrogate model predictions remains small. At the same time, the results illustrate that the modeling of the time-averaged propulsion influences by means of learned time-averaged velocity fields pursued here does not strictly enforce a divergence-free velocity field, since the target velocities are not continuity-compatible.



20  
 Figure 10: Comparison of  $x$ -velocity contours obtained from the time-averaged CFD (left) and the surrogate model (center) normalized with the ship speed in addition to the corresponding normalized error magnitude contours (right) for the test sample in the meta-grid.



21  
 Figure 11: Comparison of velocity magnitude contours obtained from the time-averaged CFD (left) and the surrogate model (center) normalized with the ship speed in addition to the corresponding normalized error magnitude contours (right) for the test sample in the meta-grid.

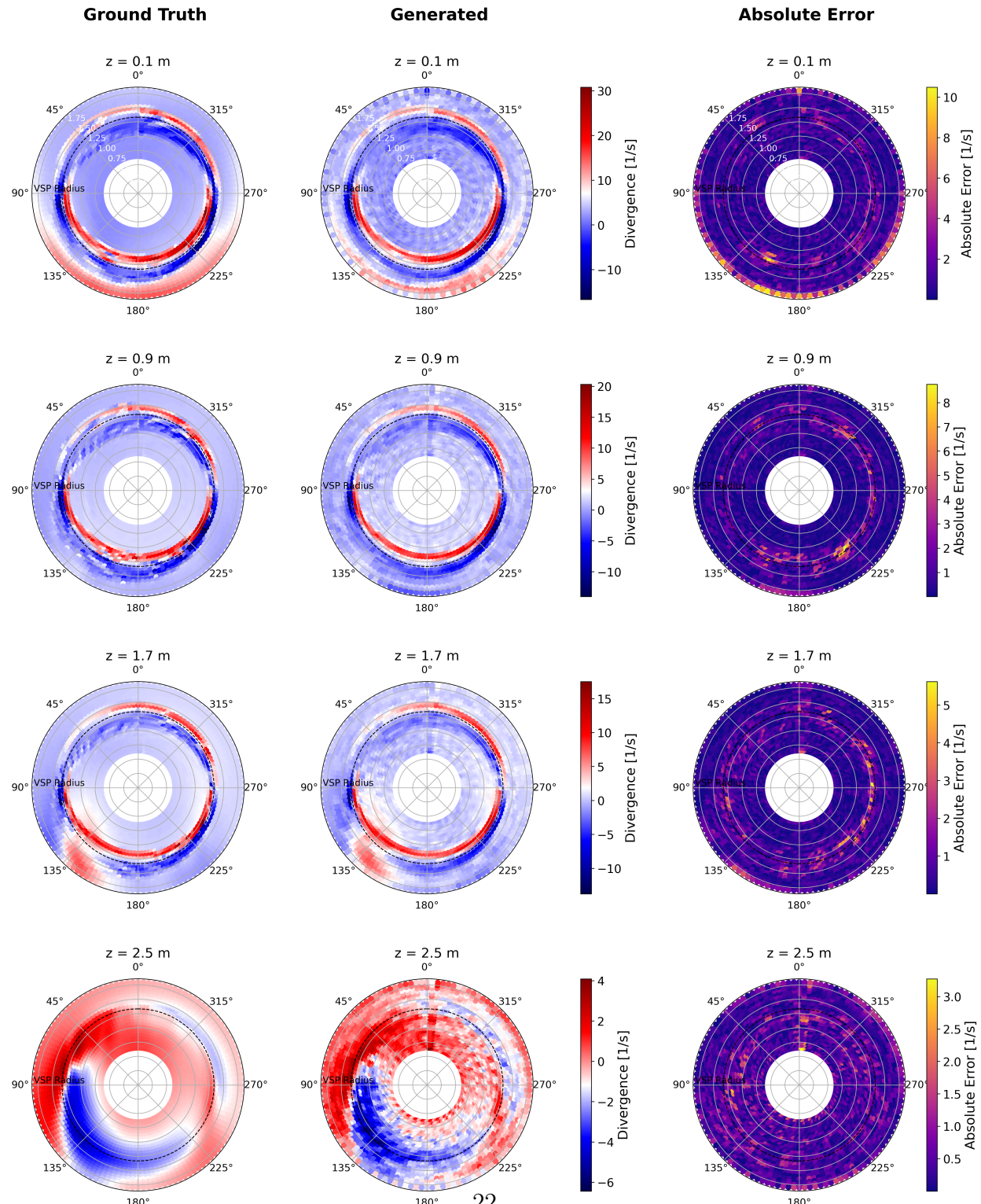


Figure 12: Comparison of velocity divergence contours obtained by 2nd-order Finite Differences from the time-averaged CFD (left) and the surrogate model (center) results with corresponding error magnitude contours (right) for a test sample in the meta-grid.

#### 4.2. Verification of Propulsion Model Integration into CFD

To verify the proposed forcing-based propulsion modeling, numerical experiments are conducted on a specific SOV geometry. The cruising speed and geometric parameters employed for these studies, which are also part of the test data, are summarized in Table 3.

Table 3: Conditioning parameters used for the test case.

Parameter	Unit	Value
Ship Speed	m/s	6.73
Stern Deadrise	deg	0.0
Stern Inclination	deg	0.4
SAY1	deg	1.88
SAY2	deg	5.29
HB_Length	-	1.0
PhiX	deg	0.0
HBAS	deg	11.95
HBH	m	0.42
HBLB	m	3.8
HBLF	m	2.12

The initial setting refers to a simulation, in which both the ship and propeller geometries are resolved in the computational domain. We refer to this as the Resolved-Propeller (RP) simulation. This employs a numerical grid as described in Section 3.2. Subsequently, the numerical grid resolving the propeller is substituted by the surrogate model, the remaining grid is refined and a set of pseudo-transient simulations are realized using a standard, pressure-based Finite Volume procedure [69] for different values of the non-dimensional forcing coefficient  $\hat{\alpha}$ . We refer to these as the Surrogate-Model (SM) simulations. The refined grid employed by the SM simulations involve approximately 1.6 million cells and targets to accurately capture near wall flow patterns in the vicinity of the ship (design). The different spatial discretizations between the RP and SM simulations are shown in Fig. 13.

Both simulation setups measure the total resistance of the hull, i.e., the total force in the main flow direction ( $x$ -direction), supplemented by area-averaged velocity components  $V_x$  extracted at two planes located slightly upstream and downstream of the propeller or surrogate model. Both planes are perpendicular to the  $x$ -direction and defined at a distance from the center

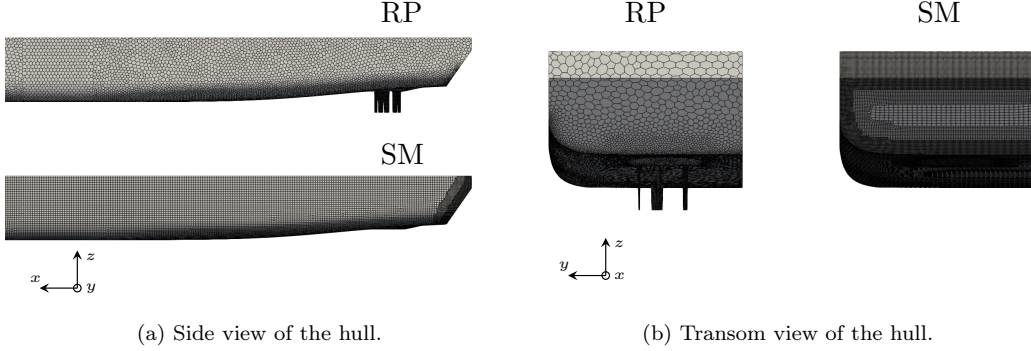
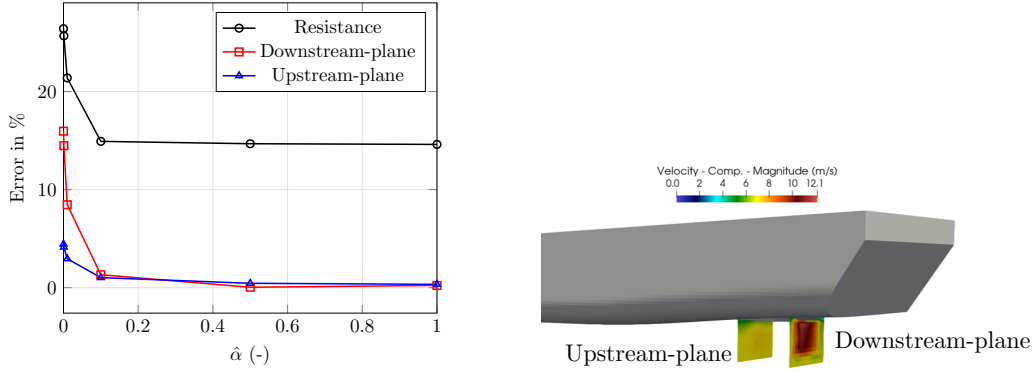


Figure 13: Spatial discretization of ship hull for the RP and SM simulations.

of the VSP of approximately  $\pm 0.75 D_{VSP}$ . The depth and width of the planes are approximately,  $L_{VSP}$  and  $1.37 D_{VSP}$ , respectively. A sketch of the planes used to compute the area-averaged velocity metrics is shown in Fig. 14b.

Figure 14a shows the percentage error of the SM results relative to the RP results, which in this context we assume they refer to the "ground truth". The error is computed as  $| (J^{SM} - J^{RP}) / J^{RP} | \cdot 100$ , where  $J$  refers to one of the metrics described above. For small forcing coefficients, all metrics result in a significant error relative to the predictions of the RP simulation. Additionally, note that  $\hat{\alpha} = 0$  corresponds to a simulation where the propeller influence is completely neglected. The error stagnates after  $\hat{\alpha} = 0.1$ , with further increases on the forcing coefficient resulting in minor changes on the predicted metrics. It is shown that as compared to a simulation in which the propeller is completely neglected ( $\hat{\alpha} = 0$ ), the proposed solution forcing approach based on the ML-based surrogate model is able to produce significantly improved predictions, at a trivial (as compared to the RP simulation) computational cost. Specifically, the error converges to approximately zero for the velocity-based metrics while it stagnates at approximately 14.5% for resistance.

While the magnitude of the latter is substantial, we would like to argue that it does not indicate a shortcoming of the surrogate model. As already discussed, the RP and SM simulations deliberately employ different grid discretizations. A comparatively coarse grid with approximately 0.9 million cells is used to discretize the domain in the RP case, excluding the mesh of the propeller. This allows us to reduce the overall offline training effort without compromising the accuracy of the propulsion data, since the propeller mesh is



(a) Resistance is shown in black line, the downstream-plane area-averaged  $x$ -velocity component in red line and the upstream-plane area-averaged  $x$ -velocity component in blue line.

(b) Sketch of the position and size of the planes used to compute the velocity metrics. Planes colored by computed velocity magnitude using the implicit forcing approach.

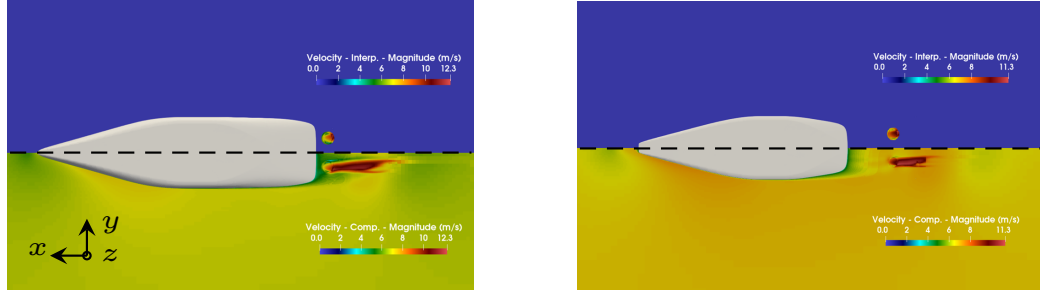
Figure 14: Verification study for the propulsion model integration into CFD. Left: Error in percentage of the SM-predicted metrics for different values of  $\hat{\alpha}$  from the RP-predicted metrics.

resolved using approximately 1.3 million cells, cf. Section 3.2. A significantly finer grid with approximately 1.6 million cells is used for the SM case. The finer discretization is particularly better resolved in the near-wall region and along the walls, in view of the subsequent optimization studies, which require an accurate estimation of velocity gradients near the walls to compute the sensitivities.

To investigate the influence of the mesh in the prediction of resistance, we performed one additional simulation using the discretization of the RP simulation without resolving the propeller. We then compared the resistance with the one predicted by the SM case for  $\hat{\alpha} = 0$ . The two cases are equivalent and the resistance-prediction differences should reduce to the spatial discretization. The relative difference, using the same formula as the one used for the error computation, is found to be 14.6%. Therefore, we argue that the error of 14.5% between the RP and the SM cases (for  $\hat{\alpha} > 0.1$ ) shown in Fig. 14a, is due to the difference in discretization strategies and not due to the the surrogate model.

Figure 15 shows the interpolated field (in the CFD mesh) and the computed velocity (in the CFD mesh) based on the employed solution forcing approach for  $\hat{\alpha} = 0.5$  at a position of 0.1 m (Fig. 15a) and 0.9 m (Fig. 15b) below the mounting point of the VSP. As shown, all key features of the

surrogate model-based flow prediction are sustained during the computation process while also being able to naturally blend the surrounding flow with the forced solution.



(a) Contour plots at  $z = 0.1\text{m}$  below the mounting point of the VSP.

(b) Contour plots at  $z = 0.9\text{m}$  below the mounting point of the VSP.

Figure 15: Velocity magnitude contours at  $0.1\text{m}$  (left) and  $0.9\text{m}$  (right) below the mounting point of the VSP. The dashed line denotes the symmetry plane. The top part is colored by the interpolated velocity magnitude coming from the surrogate model and the bottom part by the computed velocity magnitude as a result of the implicit forcing approach.

## 5. Shape Optimization Method

In the following, we describe the surrogate model shape optimization procedure considered in this work based on the employed adjoint system, the mesh deformation approach, and the handling of the additional geometric constraint. Finally an optimization algorithm for the implementation of the aforementioned is presented.

### 5.1. Adjoint System

We consider a continuous adjoint, gradient-based and parameter-free shape optimization procedure. The objective function to be minimized is the total resistance of the underwater hull, viz.,

$$J = \int_{\Gamma_O} [p^{\text{eff}} \delta_{ij} - 2\mu^{\text{eff}} S_{ij}] n_j r_i \, d\Gamma, \quad (10)$$

where  $\Gamma_O$  denotes the boundary of the underwater hull,  $n_j$  denotes the normal to the boundary and  $r_i$  refers to the main flow spatial direction, in our case the  $x$ -direction. Note that when the surrogate model is considered, the primal

solution is only solved using an unsteady setting to stabilize the solver, while in fact the solution is time-independent, due to the time-averaged velocity field coming from the surrogate model. Therefore, any temporal derivatives can be neglected. Furthermore, if the *frozen turbulence* assumption, where variations in the turbulent viscosity are neglected, is applied in deriving the dual system for Eqs. (4, 5), the adjoint field equations take the form

$$\hat{R}^p = -\frac{\partial \hat{v}_i}{\partial x_i} = 0 \quad (11)$$

$$\hat{R}_i^v = \rho \hat{v}_j \frac{\partial v_j}{\partial x_i} - \rho v_j \frac{\partial \hat{v}_i}{\partial x_j} - \frac{\partial}{\partial x_j} \left( 2\mu^{\text{eff}} \hat{S}_{ij} - \hat{p} \delta_{ij} \right) = 0, \quad (12)$$

where  $\hat{v}_i$  and  $\hat{p}$  denote the adjoint velocity components and adjoint pressure, respectively. The components of the adjoint strain-rate tensor are denoted by  $\hat{S}_{ij}$ . The system of equations is closed by the following boundary conditions for adjoint velocity and adjoint pressure,

$$\begin{aligned} \hat{v}_i &= -r_i, \quad \frac{\partial \hat{p}}{\partial x_i} n_i = 0 && \text{on the ship hull, i.e. } \Gamma_O \\ \hat{v}_i &= 0, \quad \frac{\partial \hat{p}}{\partial x_i} n_i = 0 && \text{on the inlet,} \\ \frac{\partial \hat{v}_i}{\partial x_k} n_k &= 0, \quad \hat{p} = \rho v_k n_k \hat{v}_i n_i && \text{on the outlet and} \\ \hat{v}_i n_i &= 0, \quad \frac{\partial \hat{v}_i}{\partial x_j} n_j t_i = 0, \quad \frac{\partial \hat{p}}{\partial x_i} n_i = 0 && \text{on symmetry plane and slip walls,} \end{aligned} \quad (13)$$

where  $t_i$  denotes the tangential vector to the surface. A detailed derivation of the adjoint field equations and the corresponding boundary conditions for the employed objective can be found in [9].

The system of adjoint equations is discretized using a similar FVM procedure as the one used for the primal. The adjoint pressure-velocity coupling is resolved by a method similar to the primal SIMPLE algorithm. Note that in adjoint systems, the information transfer is reversed w.r.t. the primal. To this end, the convective term is discretized by a downwind analogy to the corresponding primal discretization scheme.

After the solution of the primal and adjoint system of equations, the adjoint sensitivity can be computed as

$$s = - \int_{\Gamma_O} \mu^{\text{eff}} \frac{\partial v_i}{\partial x_j} n_j \frac{\partial \hat{v}_i}{\partial x_k} n_k d\Gamma. \quad (14)$$

The detailed derivation of Eq. (14) can be found, for instance in [70, 71]. Based on this expression, we can also define a local sensitivity that can be computed in each discretized boundary face of  $\Gamma_O$  as,

$$s^{\text{loc}} = \mu^{\text{eff}} \frac{\partial v_i}{\partial x_j} n_j \frac{\partial \hat{v}_i}{\partial x_k} n_k \quad \text{on } \Gamma_O. \quad (15)$$

Once the physical sensitivity is computed, the process continues by computing an admissible deformation field for every computational node of the mesh. A variety of different such approaches can be found in [72]. In this work, we employ the the Steklov-Poincaré method to obtain the deformation field. The latter as well as the approach to conserve the volume of the hull are outlined in [9].

The shape optimization algorithm employed in this work is summarized in Algorithm 1. In lines 1-4, the algorithm proceeds to employ the pre-trained surrogate model given the conditioning parameters, geometric and flow conditions, that relate to the optimization case. Note that the surrogate model is only employed once, outside of the main optimization loop. This implies that any changes in the geometry of the ship are not taken into account for the subsequent optimization steps. The main optimization loop (lines 5-24) incorporates an Armijo backtracking line search, which is summarized by the loop in lines 6-15. Specifically to that, the initial step size  $t^0$  is implicitly determined on the first optimization iteration by a maximum displacement approach. The algorithm then checks whether the condition in line 9 is fulfilled based on a prescribed value of  $c \in (0, 1)$  and if not, it reduces the step size by  $\tau \in (0, 1)$ . We consider the optimization converged if the relative decrease of the objective function between two consecutive steps is below  $\epsilon^{\text{conv}}$ .

Due to the parameter-free approach employed by this work, the geometry does not require re-meshing and the initial topology is sustained. This feature of the method enables

1. the consistent application of the surrogate model-based velocity field without the need of re-interpolating for each design candidate
2. restarting the primal and adjoint simulations based on the solutions of the previous iteration.

The latter results in a significant speed-up of the whole procedure since the required (pseudo) time steps for convergence of the primal problem are considerably reduced in comparison to the initial shape.

---

**Algorithm 1** Algorithm for adjoint-assisted, gradient-based, parameter-free shape optimization using a propulsion surrogate model.

---

**Require:** initial shape,  $t^0$ ,  $\epsilon^{\text{conv}} > 0$ ,  $\hat{\alpha} \geq 0$ ,  $c, \tau \in (0, 1)$ ,  $N^{\max}$ ,  $L^{\max}$

```

1: Identify conditioning parameters based on case, cf. Table 1.
2: Call surrogate model to acquire velocity field in the local meta-grid.
3: Translate and rotate the meta-grid to align with the mounting point of
   the propeller in the CFD mesh.
4: Interpolate the velocity field to the CFD mesh based on Eq. (7).
5: for  $k = 0, 1, \dots$  do
6:   for  $l = 0, 1, \dots$  do
7:     Solve the primal problem using solution forcing in the
       momentum equations, cf. Eq. (9).
8:     Evaluate objective function  $J^k$ , cf. Eq. (10).
9:     if  $(k > 0 \text{ and } J^k \leq J^{k-1} + ct^{k-1}dJ^{k-1})$  or  $(l > L^{\max})$  or  $(k = 0)$ 
   then
10:    break
11:   else
12:      $t^k \leftarrow \tau t^k$ 
13:     Reverse mesh to level  $k - 1$  and re-update based on new step
       size.
14:   end if
15:   end for
16:   if  $(k > 0 \text{ and } (|J^k - J^{k-1}|/J^{k-1}) \cdot 100 \leq \epsilon^{\text{conv}})$  or  $(k > N^{\max})$  then
17:     break
18:   end if
19:   Solve the adjoint problem, cf. Eq. (11, 12).
20:   Evaluate local sensitivity, Eq. (15).
21:   Compute descent direction based on Steklov-Poincaré method and
       volume conservation constraint, see e.g., [9].
22:   Update mesh.
23: end for

```

---

## 6. Optimization Application

The proposed surrogate model-based optimization method is applied to optimize the shape of an SOV. The initial hull geometry of the vessel corresponds to the test case investigated in Section 4.2. It is described by the

parameters in Table 3 and illustrated in Figs. 16a and 16b. Note that the headbox of the SOV, displayed in red, is not a design surface, to ensure that a plane surface is sustained during the optimization on which the VSP propeller can be properly mounted. Simulations are performed for a half model at a ship speed of  $V_s = 6.73$  m/s, resulting in a Re-number of approximately  $6.35 \cdot 10^8$ . The computational domain is discretized with approximately 1.6 million locally-refined hexahedral control volumes. Figure 16c shows the computational grid used near the hull of the ship. As shown there, the grid is progressively refined towards the ship so that to accurately predict the boundary layer along the hull. However, there is no extra artificial refinement in the area swept by the propeller.

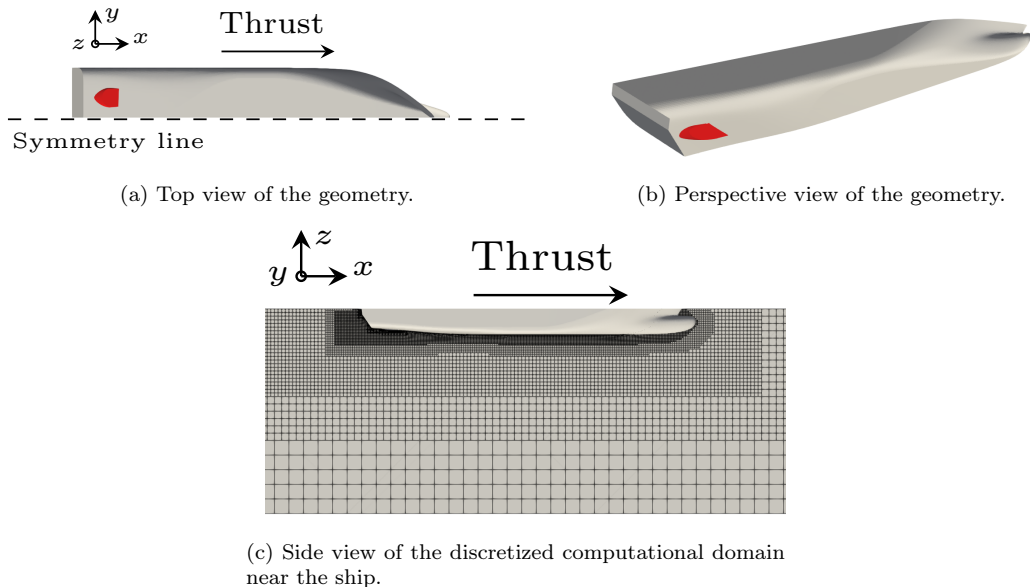


Figure 16: Initial shape and discretized computational domain. Areas of the hull that are free for design are displayed in grey while those that are fixed to their initial position are displayed with red.

A  $k-\epsilon$  Boussinesq-viscosity model is used to model turbulence. A QUICK scheme is used to discretize all convective terms while pseudo-time stepping is performed for primal convergence using an implicit Euler temporal discretization with a time step of  $\Delta t \cdot V_s / L_{OA} = 0.365 \cdot 10^{-3}$ .

In the optimization process, the initial step size is determined using a maximum displacement approach that constricts the maximum local dis-

placement on a computational face to  $d^{\max} = \text{LOA}/1000$ . Convergence is monitored by  $\epsilon^{\text{conv}} = 0.1$ . This implies that the optimization is terminated when the objective for two subsequent shapes changes by less than 0.1%. Optimization and Armijo thresholds are set to  $N^{\max} = 50$  and  $L^{\max} = 10$ , respectively. Armijo constants are set to  $c = 10^{-20}$  and  $\tau = 0.5$ , effectively checking only cases in which the objective function increases in two consecutive steps. This can happen due to the application of the volume constraint which alters the deformation field in such a way that a descent direction is not always guaranteed.

We consider two optimization cases. The first corresponds to an optimization which neglects the propeller influence and is realized by setting  $\hat{\alpha} = 0$ . We refer to this as the *No-Propeller* (NP) case. The second run employs a forcing coefficient of  $\hat{\alpha} = 0.5$ , based on the results presented in Fig. 14a. We refer to this as the *Surrogate-Propeller* (SP) case.

### 6.1. Optimization results

Figure 17 shows the computed (constrained) displacement field on the hull for the first optimization iteration for each case. Three characteristic areas can be identified as the most influential to the optimization process: the transom (leftmost part of the hull), the midship and the bow. The largest contribution is observed at the transom, regardless of the optimization case. Interestingly, when the surrogate model is considered, an additional region of high displacement appears near the propeller wake. Moreover, the displacement fields at the midship and bow also significantly differ in both their magnitude and pattern.

Figure 18a shows the relative decrease of the objective function as compared to the initial shape during the optimization process. Both cases met the imposed convergence criterion with NP reaching a decrease of approximately 2% while SP reaches a decrease of approximately 8.2%. The SP case did not satisfy the Armijo condition at iteration 12 based on the initial step size. However, after a maximum of 4 Armijo iterations, a smaller step size able to satisfy the condition was successfully identified. Figure 18b shows the relative change of the displaced water volume (volume of the hull) during the optimization. Both constrained optimization cases managed to sustain the initial volume with no changes larger than 0.15% reported.

It is additionally important to note that in Fig. 18a we show the relative decrease of each case based on their corresponding primal. This means that

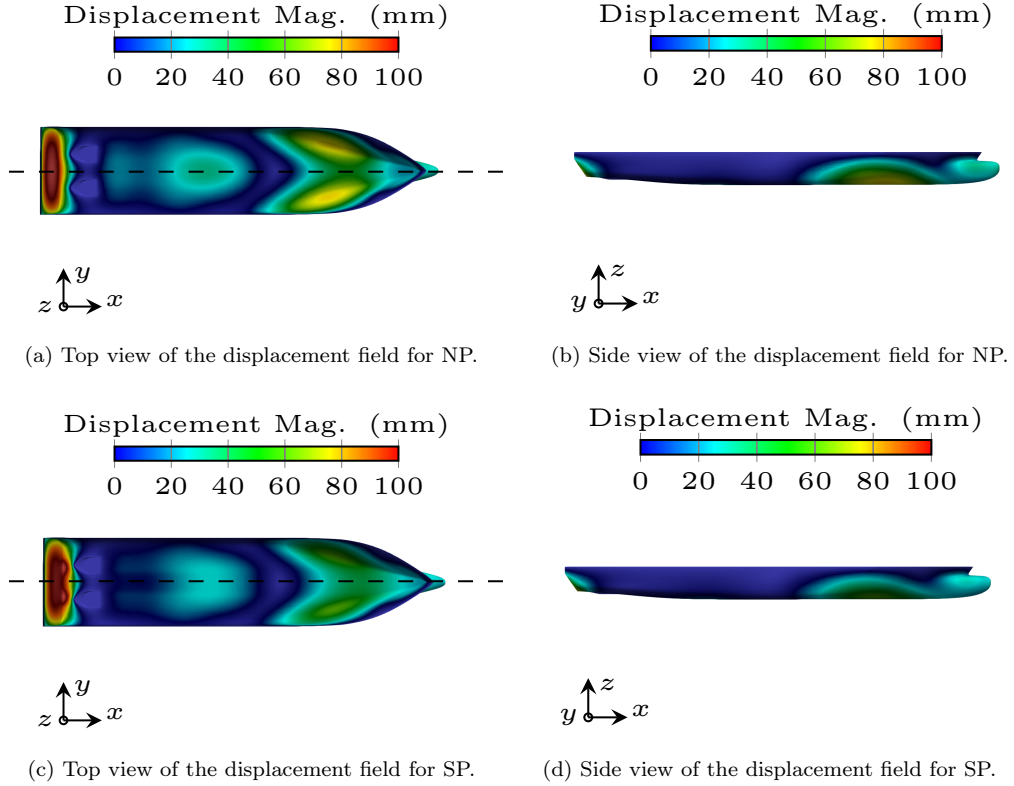


Figure 17: Displacement field computed on the hull for the first optimization iteration ( $k = 0$ ). Complete hull is used for visualization purposes. Dashed line indicates the symmetry plane.

while the SP case predicts the resistance with the use of the surrogate model, the NP prediction disregards this and thus  $J^{0,\text{NP}} \neq J^{0,\text{SP}}$ .

In Fig. 19 we show the framelines at three characteristic positions of the ship along its length. As expected by the predicted displacement field (Fig. 17), the most noticeable difference between the NP and SP cases are observed near the wake of the propeller. When a surrogate model is considered, the optimizer proceeds to create a "tunnel-like" segment behind the headbox allowing for a smoother flow transition towards the transom. Additionally, both cases resulted in a minimization of the wetted area near the  $X3$  position. Finally, the changes at the midship region were trivial as compared to  $X1$  and  $X3$ .

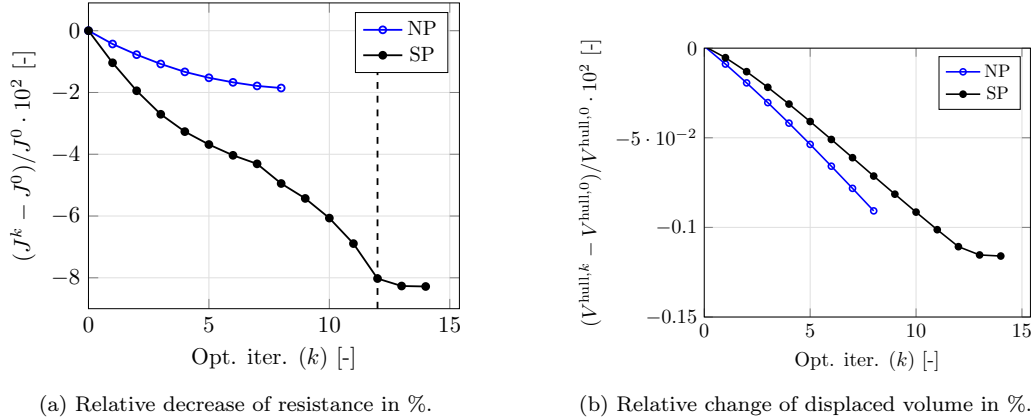


Figure 18: Optimization history. Vertical dashed lines highlight the optimization iteration in which the Armijo condition was for the first time not fulfilled.

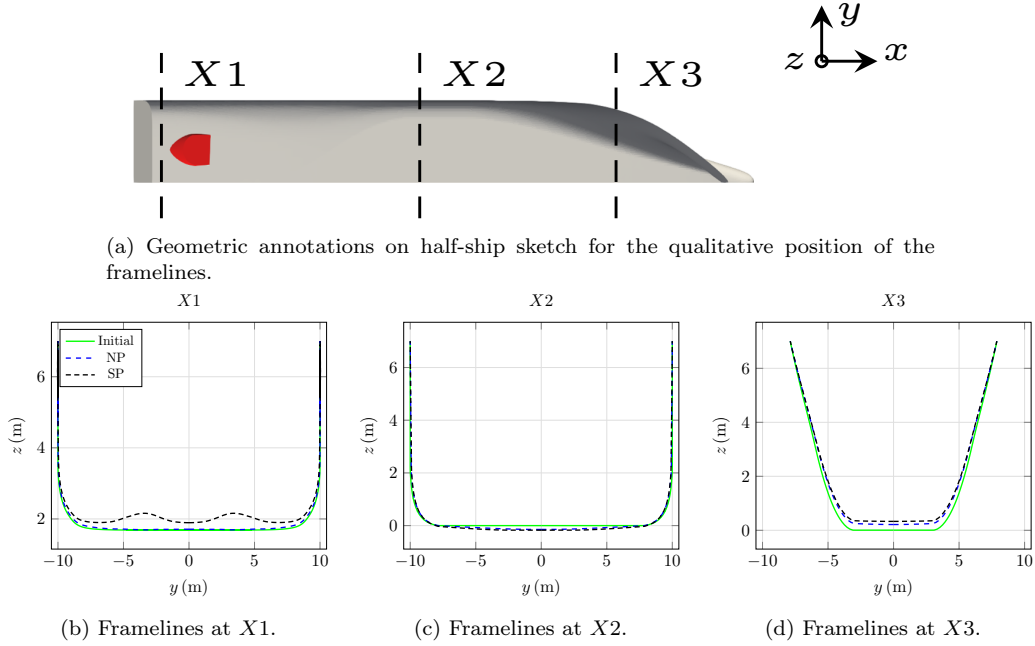


Figure 19: Framelines at three characteristic positions of the ship along its length. Continuous (green) line corresponds to the initial shape, dashed (blue) line to the optimized shape of the NP case, densely dashed (black) line to the optimized shape of the SP case. Symmetry line at  $y = 0$ .

## 6.2. Validation of the Optimization Studies

The validation of the optimization studies aims to evaluate the relevance of considering propulsion effects in studies of hull-shape optimization. For this purpose, the optimal shapes of the two optimization studies with propulsion influences (SP) and without propulsion influences (NP) are analyzed. The analysis of both shapes is based on two corresponding primal flow simulations: a transient simulation with a geometrically resolved VSP, cf. Section 3, and a steady-state simulation using the ML-based surrogate model of the VSP. Reported results are restricted to the objective functional, i.e., the hydrodynamic drag obtained from these four primary flow studies, and their comparison with the prognosis of the adjoint shape optimization.

Results obtained from the ML-based surrogate model simulations predict an **increase** in drag by approximately 3% for the shape obtained from the NP-optimization, which clearly contradict the prognosis of the optimization study, and a **decrease** of about 8.2% for the SP-optimization. Finally, the optimized shapes are assessed using transient simulations in which the propeller is explicitly resolved. The resolved-propeller simulation of the NP-optimized shape predicted a 2.26% **increase** in resistance and also clearly contradicts the optimization study. In contrast, the corresponding simulation for the SP-optimized shape predicted a 9.29% **decrease**.

Looking at the shape obtained from an optimization study that neglects propulsion influences, we note that the drag for the (supposedly) optimized hull shape actually increased by approximately 2%-3% in both simulations. This result underscores the need to include propulsion influences in a hull-shape optimization process. On the other hand, both simulations confirm a significant decrease in resistance about 8%-9 % for the hull shape derived from the optimization with propulsion. Although the relative values obtained from the resolved and ML-based propulsion simulations do not exactly agree, the overall trend is remarkably accurate considering the fundamentally different grids. This agreement reinforces the efficiency of the surrogate-model-based optimization approach, demonstrating that additional expensive high-fidelity, propeller-resolved CFD simulations are not required to confirm the optimization outcomes.

## 7. Conclusion

In this study, a parametric surrogate model for the Voith Schneider Propeller (VSP) was developed to take into account the influences of propeller-

hull interaction within a hull-shape optimization process, that aims to minimize the hydrodynamic resistance of a Service Operation Vessel (SOV) equipped with a five-bladed Voith–Schneider Propeller (VSP) in full scale. By using the data-driven surrogate model in an adjoint-based shape optimization framework, the optimization procedure can correctly mimic the propeller-hull interaction and thus gains considerable accuracy compared to an optimization without considering the surrogate model.

During the offline phase, 180 unsteady Reynolds-averaged Navier–Stokes simulations were performed and the velocity fields for each training sample were time-averaged and mapped from the unstructured CFD grids onto a structured meta-grid. Subsequently, a conditional variational autoencoder (CVAE) was developed to model the mapped three-dimensional velocity fields based on 10 geometric conditions and the cruising velocity. Residual blocks and self-attention mechanisms were incorporated into the encoder and decoder to enhance the model’s ability to capture strong local gradients. The validation of the surrogate model for unseen data reveals an excellent agreement with the time-averaged full-order model results. It was shown that the maximum relative percentage error across all slices of the trained model does not exceed 1.6% The comparison shown also demonstrates that the time-averaged velocity fields cannot be continuity-compatible because of the temporary overlap of the fields by the propeller blades. This must be taken into account during further data processing.

In the second phase, the surrogate model was used to support steady primal simulations, which are required to optimize the hull shape. To this end, the velocity field generated by the surrogate model was interpolated in a mesh of finer resolution in the vicinity of the hull that does not geometrically resolve the propeller. The machine learning-based velocity field was implicitly incorporated into the solution of the discrete momentum equations. This implicit forcing is based on local weights and yields very good agreement with the learned velocities without enforcing 100% agreement, which is undesirable due to the aforementioned continuity issues. Specifically, it was found that already for a non-dimensional forcing coefficient slightly above  $\hat{\alpha} = 0.1$  the surrogate model-based approach was able to reproduce several metrics of interest for the unsteady flow around the initial vessel under investigation, with differences being attributable to discrepancies in the spatial discretization.

Finally, the proposed methodology was integrated into a CAD-free shape optimization process consisting of sequences of primal and adjoint simulations

and applied to the SOV geometry. Our results showed that:

1. omitting the propulsion system during optimization can be detrimental. While the optimization run reported a 2% decrease of the resistance when neglecting the propulsion system, subsequent CFD simulations including the propulsor showed that the optimized ship's resistance was actually increased by approximately 3% as compared to the initial shape.
2. the surrogate model was able to identify hull geometries that lead to a decrease of the ship's resistance by more than 8%. This result was also validated by a propeller-resolved simulation.

These results highlight the importance of considering the propeller–hull interaction in adjoint-based hull optimizations and demonstrate the effectiveness of coupling data-driven surrogate models with physics-based CFD solvers.

Limitations of the displayed investigations include the “frozen” treatment of the surrogate model during optimization and the single-phase simulation approach used for the CFD and optimization simulations shown in this work. We are currently working towards updating the geometric conditions that serve as input to the surrogate model at each design candidate during an optimization run, i.e., including lines 1-4 of Algorithm 1 inside the optimization loop (lines 5-23). We also target to extend the proposed methodology to two-phase flows and self-propulsion settings that allow dynamic movement of the vessel.

## Acknowledgements

The authors would like to thank Henning Schwarz for his valuable discussions and contributions to the development of the surrogate model, as well as David Bendl for his assistance in preparing the geometries.

M.A.M. acknowledges the support of the Marie Skłodowska-Curie Actions under the HORIZON-MSCA-2021-DN-01 programme (Grant No. 101072851), through the MFLOPS (Multiphase Flow Optimisation Strategies with Industrial Applications) project. G.B., A.H., T.T.N., M.P. and T.R. acknowledge support from the "Propulsion Optimization of Ships and Appendages" (ProSA) research project funded by the German Federal Ministry for Economic Affairs and Energy (BMWE; Grant No. 03SX599C).

## Author contributions

**Moloud A. M.:** Writing – original draft, Methodology, Software, Investigation, Formal analysis, Validation; **Georgios B.:** Writing – original draft, Writing – review & editing, Methodology, Software, Investigation, Formal analysis, Validation; **Thanh T. N.:** Data curation, Investigation, Writing – review & editing, Validation; **Ahmed H.:** Software, Investigation; **Michael P.:** Supervision, Funding acquisition ; **Thomas R.:** Writing – review & editing, Supervision, Project administration, Funding acquisition.

## References

- [1] U. N. C. on Trade, Development, Review of Maritime Transport 2023: Towards a Green and Just Transition, United Nations, Geneva, 2023, accessed: 2025-06-13. doi:10.18356/9789213584569.
- [2] T. Smith, J. Jalkanen, B. Anderson, J. Corbett, J. Faber, S. Hanayama, L. Aldous, et al., Third imo ghg study.2014, International Maritime Organization, cO<sub>2</sub> emissions: 796.Mt (international, 2012); 885.Mt (international, 2007); average 2007–2012.846.Mt (international) and 1,015.Mt (total shipping) (2015).
- [3] E. A. Bouman, E. Lindstad, A. I. Rialland, A. H. Strømman, State-of-the-art technologies, measures, and potential for reducing ghg emissions from shipping—a review, *Transportation Research Part D: Transport and Environment* 52 (2017) 408–421.
- [4] G. J. Lee, Self-similarity in the equation of motion of a ship, *International Journal of Naval Architecture and Ocean Engineering* 6 (2) (2014) 333–346. doi:<https://doi.org/10.2478/IJNAOE-2013-0183>.
- [5] A. Papanikolaou, *Ship design: methodologies of preliminary design*, Springer, 2014.
- [6] D. H. Kim, K. S. Yang, Shape optimization of a ship hull to reduce total resistance using parametric modification and cfd analysis, *International Journal of Naval Architecture and Ocean Engineering* 4 (2) (2012) 163–175. doi:10.3744/JNAOE.2012.4.2.163.
- [7] A. Stück, J. Kröger, T. Rung, Adjoint-Based Hull Design for Wake Optimisation, *Ship Technology Research* 58 (1) (2011) 34–44.

- [8] J. Springer, J. Kröger, M. Brenner, Schrader, T. L.-U., Rung, Simulation-Based Shape Optimisation of an Offshore Supply Vessel, in: International Conference on Computational Methods in Marine Engineering, ECCOMAS MARINE 2017, Nantes, France, 2017.
- [9] N. Kühl, T. T. Nguyen, M. Palm, D. Jürgens, T. Rung, Adjoint node-based shape optimization of free-floating vessels, *Structural and multi-disciplinary optimization* 65 (9) (2022) 247.
- [10] M. Giles, N. Pierce, M. Giles, N. Pierce, Adjoint equations in cfd-duality, boundary conditions and solution behaviour, in: 13th computational fluid dynamics conference, 1997, p. 1850.
- [11] J. Springer, K. Urban, Adjoint-based optimization for rigid body motion in multiphase navier–stokes flow, *SIAM Journal on Scientific Computing* 37 (2) (2015) B185–B214.
- [12] A. Nazemian, P. Ghadimi, A. Ghadimi, Shape optimization of a submerged 2d hydrofoil and improvement of its lift-to-drag ratio using cfd-based mesh morphing-adjoint algorithm, *Zeszyty Naukowe Akademii Morskiej w Szczecinie* (2022).
- [13] A. Nazemian, P. Ghadimi, Shape optimisation of trimaran ship hull using cfd-based simulation and adjoint solver, *Ships and Offshore Structures* 17 (2) (2022) 359–373.
- [14] M. Brenner, S. Harries, J. Kröger, T. Rung, Parametric-adjoint approach for the efficient optimization of flow-exposed geometries, in: MARINE VI: proceedings of the VI International Conference on Computational Methods in Marine Engineering, CIMNE, 2015, pp. 230–241.
- [15] N. Kühl, J. Kröger, M. Siebenborn, M. Hinze, T. Rung, Adjoint Complement to the Volume-of-Fluid Method for Immiscible Flows, *Journal of Computational Physics* 440 (2021) 110411. doi:10.1016/j.jcp.2021.110411.
- [16] N. Kühl, Elliptic relaxation strategies to support numerical stability of segregated continuous adjoint flow solvers, arXiv preprint arXiv:2501.12518 (2025).

- [17] Voith GmbH & Co. KGaA, Marine technology, <https://www.voith.com>.
- [18] D. Jürgens, M. Palm, Voith schneider propeller – an efficient propulsion system for dp controlled vessels, in: Proceedings of the Dynamic Positioning Conference, Voith Turbo Schneider Propulsions, Thrusters, October 13–14, 2009, 2009, heidenheim, Germany.
- [19] Voith Turbo Marine GmbH & Co. KG, The Voith Schneider Propeller: Current Applications and New Developments, Voith Turbo Marine GmbH & Company KG, 2006.
- [20] J. Hu, Q. Yan, J. Ding, S. Sun, Numerical study on transient four-quadrant hydrodynamic performance of cycloidal propellers, *Engineering Applications of Computational Fluid Mechanics* 16 (1) (2022) 1813–1832.
- [21] E. Esmailian, H. Ghassemi, S. A. Heidari, Numerical investigation of the performance of voith schneider propulsion, *American Journal of Marine Science* 2 (3) (2014) 58–62.
- [22] D. Jürgens, H.-J. Heinke, Voith schneider propeller (vsp)-investigations of the cavitation behaviour, in: First International Symposium on Marine Propulsion. Trondheim, Norway, 2009.
- [23] T. Li, S. Sun, Numerical study on the scale effects of two-dimensional cycloidal propellers, *Ocean Engineering* 279 (2023) 114445.
- [24] A. Halder, C. Walther, M. Benedict, Hydrodynamic modeling and experimental validation of a cycloidal propeller, *Ocean Engineering* 154 (2018) 94–105.
- [25] A. Griewank, A. Walther, Revolve - Reverse or Adjoint Mode of Computational Differentiation, *Transaction on Mathematical Software* 26 (1) (2000) 19–45.
- [26] M. Hinze, J. Sternberg, A-Revolve: An Adaptive Memory-and Run-Time-Reduced Procedure for Calculating Adjoints; With an Application to the Instationary Navier–Stokes System, *Optimization Methods Software* 20 (6) (2005) 645–663. doi:10.1080/10556780410001684158.

- [27] W. Symes, Reverse time migration with optimal checkpointing, *Geophysics* 72 (2007) SM213–SM221.
- [28] Q. Wang, P. Moin, G. Iaccarino, Minimal repetition dynamic checkpointing algorithm for unsteady adjoint calculation, *SIAM J. Scientific Computing* 31 (2009) 2549–2567.
- [29] L. Sirovich, Turbulence and the dynamics of coherent structures. Parts I–III, *Quart. Appl. Math.* 45 (1987) 561–571. doi:10.1090/qam/910462.
- [30] M. Brand, Incremental singular value decomposition of uncertain data with missing values, In: *European Conference on Computer Vision* 91 (2002) 707–720.
- [31] M. Brand, Fast low-rank modifications of the thin singular value decomposition, *Linear algebra and its applications* 415 (2006) 20–30.
- [32] H. Fareed, J. Singler, Y. Zhang, J. Shen, Incremental Proper Orthogonal Decomposition for PDE Simulation Data, *Computers & Mathematics with Applications* 75 (6) (2018) 1942–1960. doi:10.1016/j.camwa.2017.09.012.
- [33] H. Fareed, J. Singler, A note on Incremental POD Algorithms for Continuous Time Data, *Applied Numerical Mathematics* 144 (2019) 223–233. doi:10.1016/j.apnum.2019.04.020.
- [34] H. Fareed, J. Singler, Error Analysis of an Incremental Proper Orthogonal Decomposition Algorithm for PDE Simulation Data, *Journal of Computational and Applied Mathematics* 368 (2020) 112525. doi:10.1016/j.cam.2019.112525.
- [35] C. Vezyris, E. Papoutsis-Kiachagias, K. Giannakoglou, On the Incremental Singular Value Decomposition Method to Support Unsteady Adjoint-Based Optimization, *International Journal for Numerical Methods in Fluids* 91 (7) (2019) 315–331.
- [36] A.-S. I. Margetis, E. M. Papoutsis-Kiachagias, K. C. Giannakoglou, Reducing memory requirements of unsteady adjoint by synergistically using check-pointing and compression, *International Journal for Numerical Methods in Fluids* 95 (1) (2023) 23–43. doi:10.1002/fld.5136.

- [37] N. Kühl, H. Fischer, M. Hinze, T. Rung, An incremental singular value decomposition approach for large-scale spatially parallel & distributed but temporally serial data applied to technical flows, *Computer Physics Communications* 296 (2024) 109022. doi:10.1016/j.cpc.2023.109022.
- [38] J. Luo, R. Issa, A. Gosman, Prediction of impeller induced flows in mixing vessels using multiple frames of reference, *8th European conference on mixing* 76 (2) (194) 549–556. doi:10.1205/026387698524721.
- [39] L. Vorspel, B. Stoevesandt, J. Peinke, Optimize rotating wind energy rotor blades using the adjoint approach, *Applied Sciences* 8 (7) (2018). doi:10.3390/app8071112.
- [40] J. Park, B. G. Knight, Y. Liao, M. Mangano, B. Pacini, K. J. Maki, J. R. Martins, J. Sun, Y. Pan, Cfd-based design optimization of ducted hydrokinetic turbines, *Scientific Reports* 13 (1) (2023) 17968.
- [41] P. He, G. Filip, J. R. Martins, K. J. Maki, Design optimization for self-propulsion of a bulk carrier hull using a discrete adjoint method, *Computers & Fluids* 192 (2019) 104259.
- [42] R. Vinuesa, Perspectives on predicting and controlling turbulent flows through deep learning, *Physics of Fluids* 36 (3) (2024).
- [43] K. Duraisamy, G. Iaccarino, H. Xiao, Turbulence modeling in the age of data, *Annual review of fluid mechanics* 51 (1) (2019) 357–377.
- [44] S. L. Brunton, B. R. Noack, P. Koumoutsakos, Machine learning for fluid mechanics, *Annual review of fluid mechanics* 52 (1) (2020) 477–508.
- [45] S. L. Brunton, J. Nathan Kutz, K. Manohar, A. Y. Aravkin, K. Morgansen, J. Klemisch, N. Goebel, J. Buttrick, J. Poskin, A. W. Blom-Schieber, T. Hogan, D. McDonald, Data-driven aerospace engineering: Reframing the industry with machine learning, *AIAA Journal* 59 (8) (2021) 2820–2847. doi:10.2514/1.J060131.
- [46] N. Thuerey, P. Holl, M. Mueller, P. Schnell, F. Trost, K. Um, Physics-based deep learning, *arXiv preprint arXiv:2109.05237* (2021).
- [47] M. Raissi, P. Perdikaris, G. Karniadakis, Physics-informed neural networks: A deep learning framework for solving forward

and inverse problems involving nonlinear partial differential equations, *Journal of Computational Physics* 378 (2019) 686–707. doi:<https://doi.org/10.1016/j.jcp.2018.10.045>.

- [48] H. Eivazi, M. Tahani, P. Schlatter, R. Vinuesa, Physics-informed neural networks for solving reynolds-averaged navier–stokes equations, *Physics of Fluids* 34 (7) (2022) 075117. doi:[10.1063/5.0095270](https://doi.org/10.1063/5.0095270).
- [49] B. Liu, Y. Wang, T. Rabczuk, T. Olofsson, W. Lu, Multi-scale modeling in thermal conductivity of polyurethane incorporated with phase change materials using physics-informed neural networks, *Renewable Energy* 220 (2024) 119565.
- [50] L. Agostini, Exploration and Prediction of Fluid Dynamical Systems using Auto-Encoder Technology, *Physics of Fluids* 32 (6) (2020) 067103. doi:[10.1063/5.0012906](https://doi.org/10.1063/5.0012906).
- [51] R. Swischuk, L. Mainini, B. Peherstorfer, K. Willcox, Projection-Based Model Reduction: Formulations for Physics-Based Machine Learning, *Computers & Fluids* 179 (2019) 704–717. doi:[10.1016/j.compfluid.2018.07.021](https://doi.org/10.1016/j.compfluid.2018.07.021).
- [52] R. Pache, T. Rung, Data-driven surrogate modeling of aerodynamic forces on the superstructure of container vessels, *Engineering applications of computational fluid mechanics* 16 (1) (2022) 746–763.
- [53] Y.-E. Kang, S. Yang, K. Yee, Physics-aware reduced-order modeling of transonic flow via  $\beta$ -variational autoencoder, *Physics of Fluids* 34 (7) (2022) 076103. arXiv:[https://pubs.aip.org/aip/pof/article-pdf/doi/10.1063/5.0097740/16645667/076103\\_1\\_online.pdf](https://pubs.aip.org/aip/pof/article-pdf/doi/10.1063/5.0097740/16645667/076103_1_online.pdf), doi:[10.1063/5.0097740](https://doi.org/10.1063/5.0097740).  
URL <https://doi.org/10.1016/j.compfluid.2025.106837>
- [54] M. Loft, H. Schwarz, T. Rung, Data-driven pressure field prediction for ships in regular sea states, *Engineering Applications of Computational Fluid Mechanics* 19 (1) (2025).
- [55] H. Schwarz, M. Überrück, J.-P. M. Zemke, T. Rung, Machine learning based prediction of ditching loads, *AIAA journal* 63 (5) (2025) 1835–1854.

[56] J. Liu, G. Yang, X. Li, S. Hao, Y. Guan, Y. Li, A deep generative model based on cnn-cvae for wind turbine condition monitoring, *Measurement Science and Technology* 34 (3) (2022) 035902.

[57] C. Doersch, Tutorial on variational autoencoders (2021). arXiv:1606.05908.  
URL <https://arxiv.org/abs/1606.05908>

[58] D. P. Kingma, M. Welling, Auto-encoding variational bayes, *CoRR* abs/1312.6114 (2014).

[59] I. Higgins, L. Matthey, A. Pal, C. P. Burgess, X. Glorot, M. M. Botvinick, S. Mohamed, A. Lerchner, beta-vae: Learning basic visual concepts with a constrained variational framework, in: *International Conference on Learning Representations*, 2016.  
URL <https://api.semanticscholar.org/CorpusID:46798026>

[60] X. Wang, R. Girshick, A. Gupta, K. He, Non-local neural networks, in: *Proceedings of the IEEE Conference on Computer Vision and Pattern Recognition (CVPR)*, 2018.

[61] A. Vaswani, N. Shazeer, N. Parmar, J. Uszkoreit, L. Jones, A. N. Gomez, Ł. Kaiser, I. Polosukhin, Attention is all you need, *Advances in neural information processing systems* 30 (2017).

[62] J. Peng, R. Wang, K. Wang, H. Xiao, Attention-enhanced neural network models for turbulence simulation, *Physics of Fluids* 33 (9) (2021) 095117.

[63] P. Wu, S. Gong, K. Pan, F. Qiu, W. Feng, C. Pain, Reduced order model using convolutional auto-encoder with self-attention, *Physics of Fluids* 33 (7) (2021).

[64] K. He, X. Zhang, S. Ren, J. Sun, Deep residual learning for image recognition, in: *Proceedings of the IEEE conference on computer vision and pattern recognition*, 2016, pp. 770–778.

[65] L. N. Smith, N. Topin, Super-convergence: Very fast training of neural networks using large learning rates, in: *Artificial intelligence and machine learning for multi-domain operations applications*, Vol. 11006, SPIE, 2019, pp. 369–386.

- [66] D. P. Kingma, J. Ba, Adam: A method for stochastic optimization, arXiv preprint arXiv:1412.6980 (2014).
- [67] J. H. Ferziger, M. Peric, R. L. Street, Computational Methods for Fluid Dynamics, 4th Edition, Springer Nature, 2020, Ch. 13, pp. 537–538. doi:10.1007/978-3-319-99693-6.
- [68] M. Loft, H. Schwarz, T. Rung, Data-driven pressure field prediction for ships in regular sea states, *Engineering Applications of Computational Fluid Mechanics* 19 (1) (2025) 2553337.
- [69] T. Rung, K. Wöckner, M. Manzke, J. Brunswig, C. Ulrich, A. Stück, Challenges and Perspectives for Maritime CFD Applications, *Jahrbuch der Schiffbautechnischen Gesellschaft* 103 (2009) 127–139.
- [70] C. Othmer, A continuous adjoint formulation for the computation of topological and surface sensitivities of ducted flows, *International Journal for Numerical Methods in Fluids* 58 (2008) 861–877.
- [71] N. Kühl, P. M. Müller, A. Stück, M. Hinze, T. Rung, Decoupling of control and force objective in adjoint-based fluid dynamic shape optimization, *AIAA Journal* 57 (9) (2019) 4110–4114.
- [72] L. Radtke, G. Bletsos, N. Kühl, T. Suchan, T. Rung, A. Düster, K. Welker, Parameter-Free Shape Optimization: Various Shape Updates for Engineering Applications, *Aerospace* 10 (9) (2023).